

Supplementary Information

Supplementary Notes

**Note S1.** Description of assumptions made when developing the temperature and potential-dependent diurnal product output model.

The following assumptions were used to develop the temperature and potential-dependent diurnal product output model:

- For the Si photovoltaic module, we assumed negligible series resistance, large shunt resistance, diode ideality factor  $n = 1$  under the Shockley-Queisser (SQ) limit.
- For calculating the solar cell temperature, we assumed that the Faiman module temperature model<sup>1</sup> is an accurate model within our range of meteorological data. This equation accounts for heating due to solar irradiation (assuming an absorption constant,  $\alpha = 1$ , by the SQ limit) and the angle of irradiance, ambient temperature, efficiency of the photovoltaic module, convective heat transfer coefficients, and wind speed. Heat transfer coefficients are sourced from least squares regression fits from the Faiman model.
- For the experimental data that is inputted into the model, we assumed that the catalyst maintains its initial activity and selectivity (e.g., the ideal case). To model degradation of catalyst performance, we assumed percentage losses in ethylene selectivity during each 24 h period until a minimum threshold of performance is reached, at which point it is assumed that the catalyst is replaced (during the night, when solar irradiation = 0). For example, in one scenario we assumed that ethylene activity is lost at a rate of 1% per 24 h period until the activity reaches 80% of its original value.
- When using bulk electrolyte temperature as a proxy for ambient temperature, we assumed that the temperature in the electrochemical cell, specifically in the catholyte and at the cathode surface, is equal to the ambient temperature recorded in the meteorological data.
- For modeling the effect of diurnal irradiation only, we utilized smoothing spline regression to represent the data between discrete points. Error was interpolated using a modified Akima piecewise cubic Hermite interpolation to interpolate the measured experimental error. Modified Akima interpolation was used because it is resistant to random fluctuations between values present in normal spline models.
- When modeling the combined effect of diurnal irradiation and ambient temperature changes, we assumed a locally weighted smoothing linear regression within the range of the five tested temperatures. We did not utilize the model to extrapolate outside of this range due to potential inaccuracies in extrapolation. To model error, we employed biharmonic spline interpolation as a function of cathode potential and temperatures; this interpolation method preserves curve shapes well compared to other 3D interpolant models.
- When scaling the electrochemical device from 1 cm<sup>2</sup> for the 1 MW solar farm (~300 m<sup>2</sup>) it is assumed that the device maintains identical selectivity and activity.
- If the solar irradiance = 0 W/m<sup>2</sup> or the ambient temperature,  $T_a < 5$  °C or  $T_a > 48.5$  °C, we assumed that the device will not operate due to physical limitations. Under these conditions, all device activity is set to zero (e.g., current density).
- All reported current densities are normalized to the electrolyzer cathode area of 1 cm<sup>2</sup>.

**Note S2.** Calculation of scaled 1 MW PV-EC CO<sub>2</sub>R annual product output.

Assuming the modeled c-Si PV has the following characteristics:

- Maximum power (1000 W/m<sup>2</sup>, 25 °C) = 346.95 mW
- V<sub>oc</sub> (6 cell module) = 4.1 V
- Area<sub>1-cell</sub> = 2.29 cm<sup>2</sup>
- Area<sub>6-cell</sub> = 13.74 cm<sup>2</sup>

The 1 MW scaling factor is calculated by:

$$S.F. = \frac{10^6 W}{346.9502 \text{ mW} * \frac{1 \text{ W}}{1000 \text{ mW}}} = 2,882,258 \quad (\text{S2.1})$$

The average daily C<sub>2</sub>H<sub>4</sub> mol production is calculated by:

$$n_{C2H4} \left( \frac{\text{mol}}{\text{day}} \right) = j_{ave} \left( \frac{A}{\text{cm}^2} \right) * 1 \text{ cm}^2 * 86,400 \frac{\text{s}}{\text{day}} * \frac{1 \text{ mol e}^-}{96,485 \text{ C}} * \frac{1 \text{ mol C}_2\text{H}_4}{12 \text{ mol e}^-} \quad (\text{S2.2})$$

The average daily C<sub>2</sub>H<sub>4</sub> production (kg) for a 1 MW solar farm is calculated by:

$$kg_{C2H4} \left( \frac{\text{kg}}{\text{day}} \right) = n_{C2H4} \left( \frac{\text{mol}}{\text{day}} \right) * 28.05 \frac{\text{g}}{\text{mol}} * S.F.* 10^{-3} \quad (\text{S2.3})$$

The annual C<sub>2</sub>H<sub>4</sub> generation (tonne/yr) for a 1 MW solar farm is calculated by:

$$\text{Annual C}_2\text{H}_4 \text{ generation } \left( \frac{\text{tonne}}{\text{yr}} \right) = \sum_{i=1}^{365} kg_{C2H4} * 10^{-3} \quad (\text{S2.4})$$

## Supplementary Figures

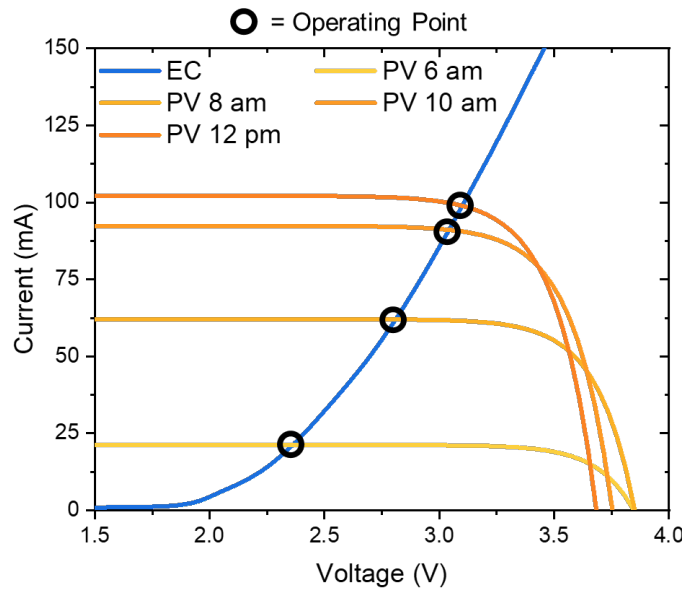


**Figure S1.** Representation of variable operating points throughout the day, with PV polarization curves calculated for the Summer solstice at 6 am, 8 am, 10 am, and 12 pm, overlaid with the electrochemical polarization curve of the  $\text{Cu}_{\text{S},\text{HL}}$  catalyst. The operating point corresponds to the intersection of the EC polarization curve and PV polarization curve for a given time.

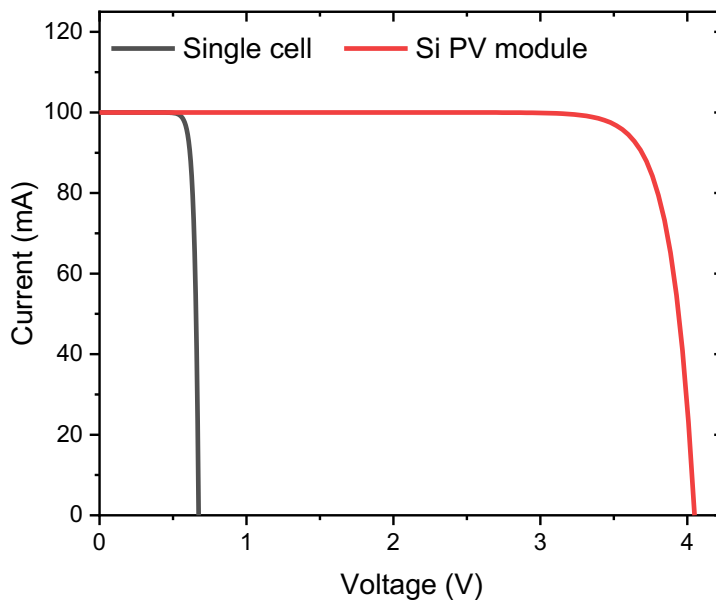


**Figure S2.** I-V behavior of a single Si solar cell (black) and the Si PV module (red), which consists of six individual solar cells connected in series. This curve acts as an operating constraint for the electrochemical  $\text{CO}_2\text{R}$  device.

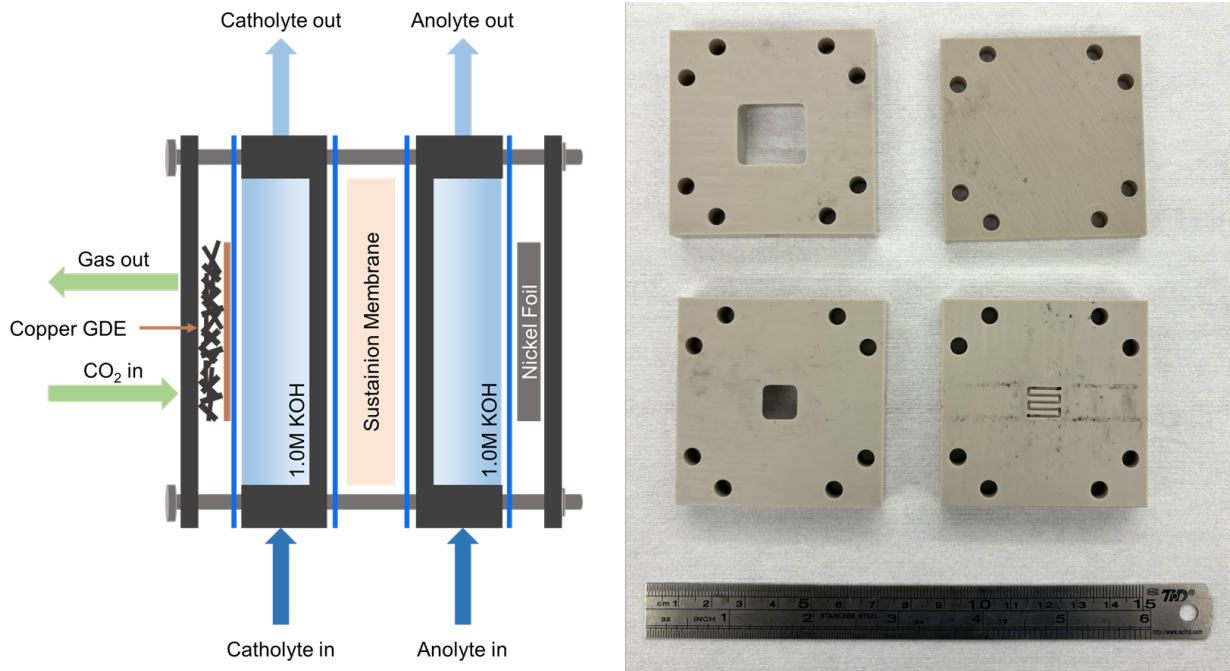


**Figure S3.** Schematic of the gas diffusion electrode flow cell and a picture of the actual flow cell used in this work. The cathode working electrode area is  $1\text{ cm}^2$  and the anode counter electrode area is  $4\text{ cm}^2$ . The anode is oversized to reduce the overpotential required to drive the oxygen evolution reaction.  $\text{CO}_2$  is fed into the cathode through a serpentine flow channel at a flow rate of  $10\text{ sccm}$  and gas products exit from the top of this channel. The catholyte and anolyte reservoirs were separated by a Sustainion anion exchange membrane and each contained  $13\text{ mL}$  of  $1.0\text{ M KOH}$  which was circulated through the electrochemical cell at  $2\text{ mL min}^{-1}$ . An Ag/AgCl reference electrode was inserted into the cathode chamber.

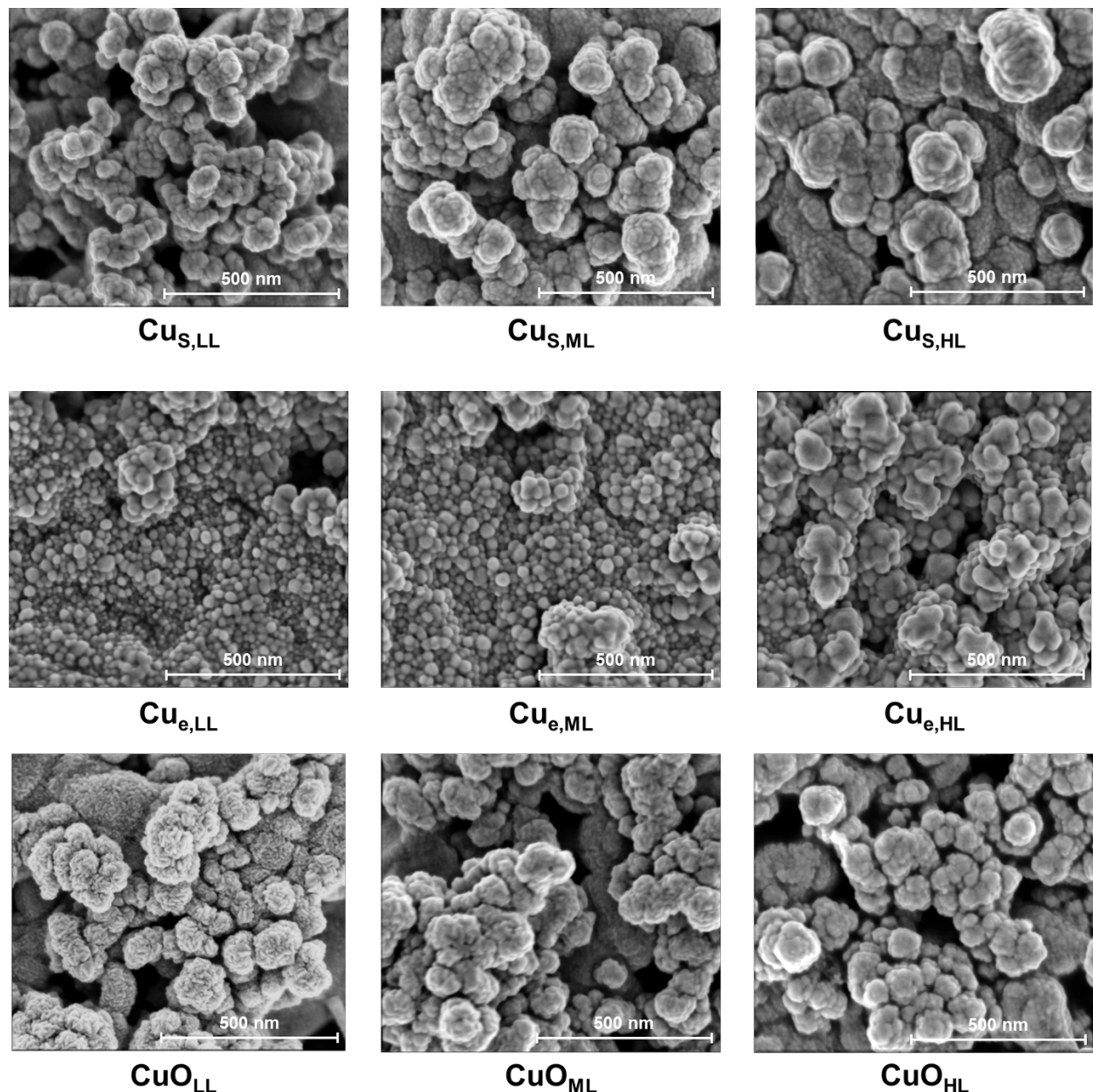


**Figure S4.** Characterization of samples chosen to control CO<sub>2</sub> reduction selectivity using morphology, loading, and composition. (A) SEM images of nine as-fabricated Cu-based electrocatalysts.

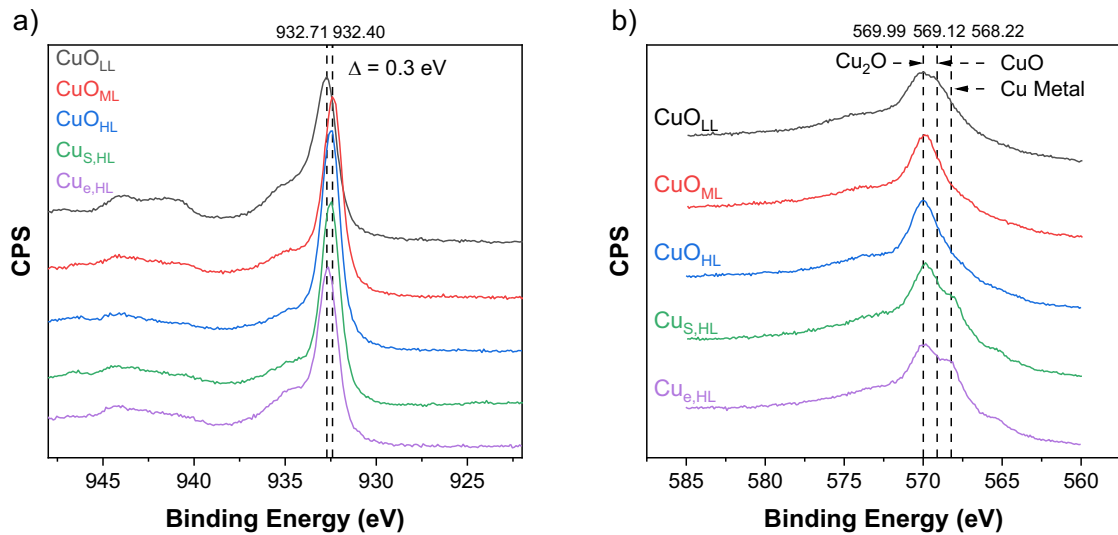


**Figure S5.** High-resolution XPS for the surface of five of the Cu-based catalysts. (A) High-resolution XPS of the  $\text{Cu}2\text{p}_{3/2}$  peak for the three  $\text{CuO}$  samples and a representative spectrum for  $\text{Cu}_s$  and  $\text{Cu}_e$  samples. (B) High resolution XPS of the Cu LMM peak for the three  $\text{CuO}$  samples and a representative spectrum for the  $\text{Cu}_s$  and  $\text{Cu}_e$  samples. **Figures S6-7** give high-resolution XPS fitting for the  $\text{Cu}_s$  family and the three  $\text{Cu}_{\text{HL}}$  samples.

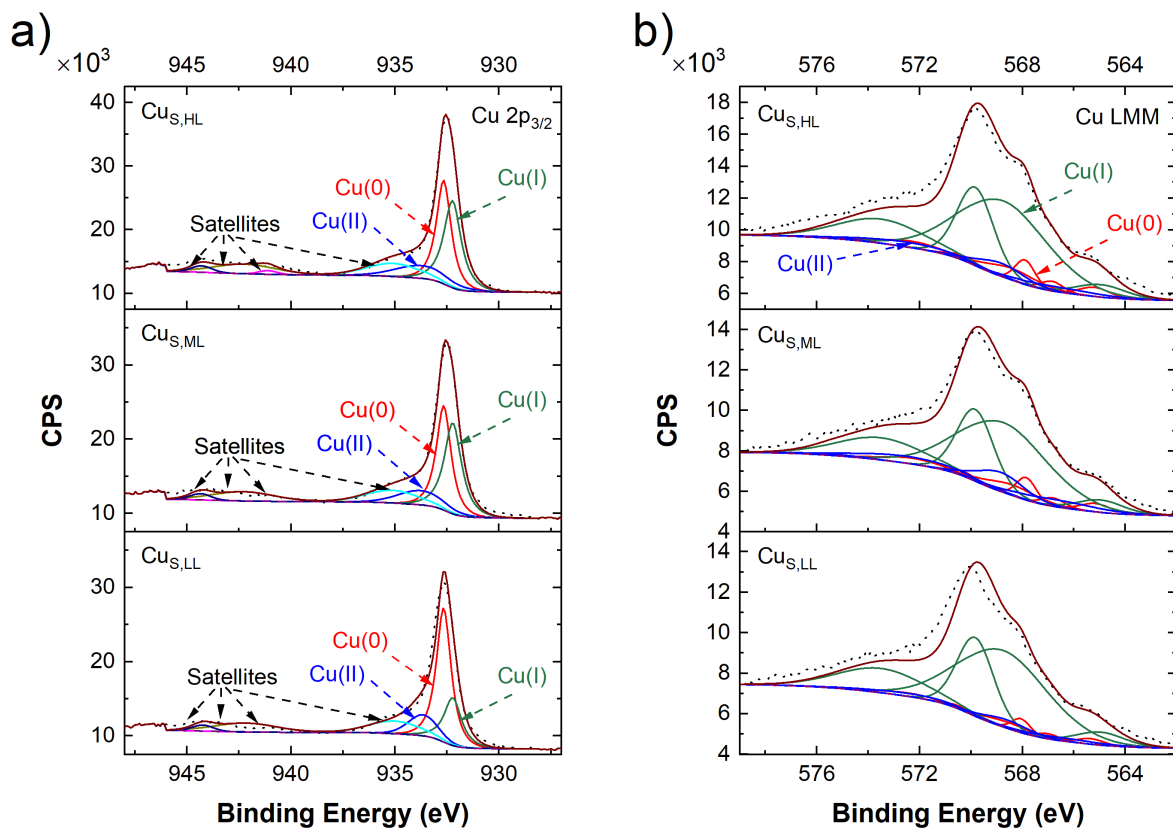


**Figure S6.** High-resolution XPS and associated fitting for the surface of the  $\text{Cu}_s$  samples. (A)  $\text{Cu}2\text{p}_{3/2}$ , (B)  $\text{Cu LMM}$ . The XPS spectra indicate that a mix of  $\text{Cu}(0)$ ,  $\text{Cu}(\text{I})$ , and  $\text{Cu}(\text{II})$  is present, which we associate with sample oxidized upon exposure to air.<sup>2,3</sup>

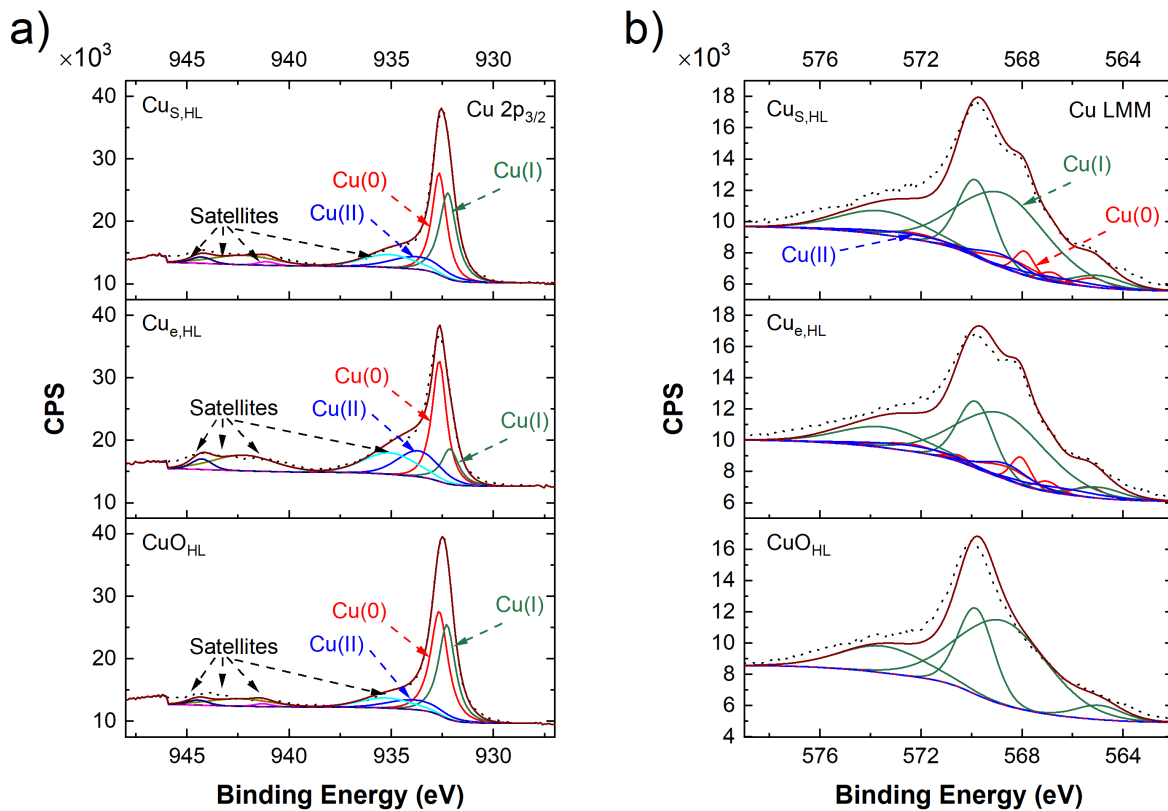


**Figure S7.** High-resolution XPS and associated fits for the surface of the HL samples from each of the three catalyst ‘families’. (A) Cu2p<sub>3/2</sub>, (B) Cu LMM. The XPS spectra indicate that the Cu(I) oxidation state is heavily present in the CuO<sub>HL</sub> sample, and is less dominant in the Cu<sub>s</sub> and Cu<sub>e</sub> samples.<sup>2,3</sup>

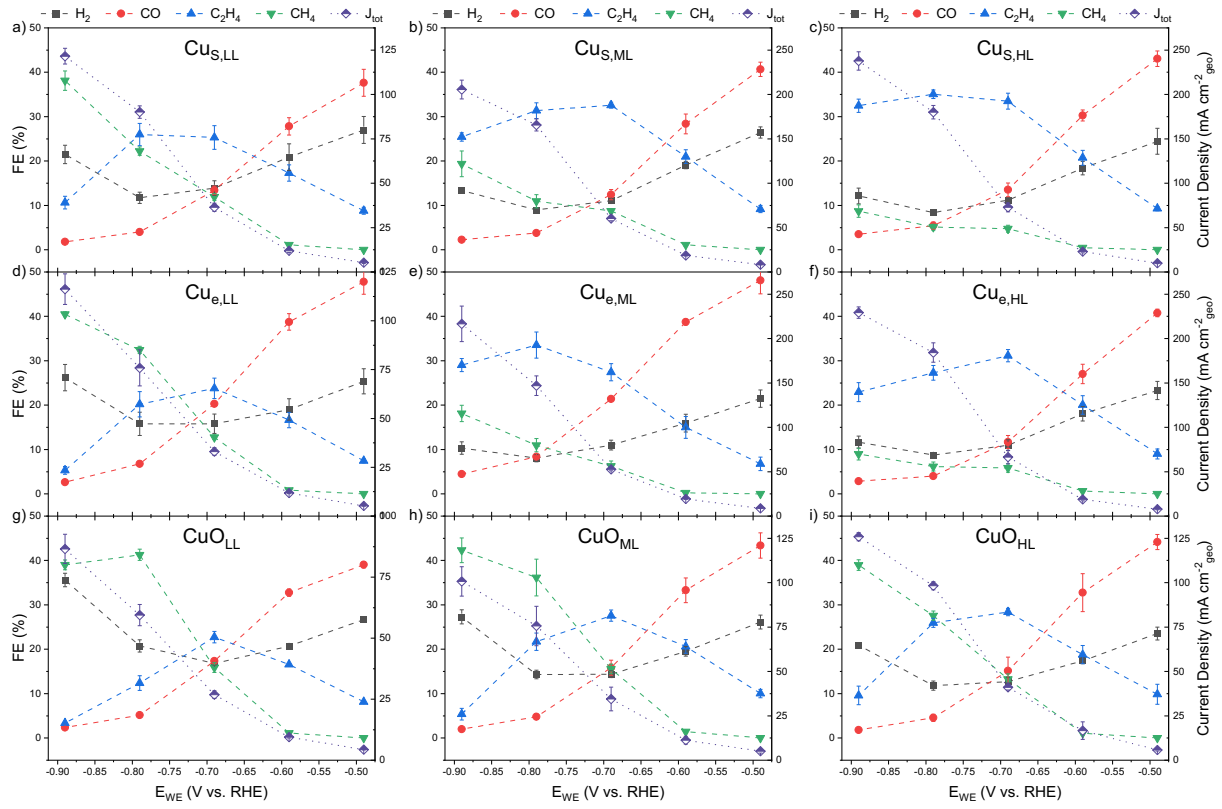


**Figure S8.** Faradaic efficiency (FE) of the individual electrocatalysts: (a)  $\text{Cu}_{\text{S},\text{LL}}$ , (b)  $\text{Cu}_{\text{S},\text{ML}}$ , (c)  $\text{Cu}_{\text{S},\text{HL}}$ , (d)  $\text{Cu}_{\text{e},\text{LL}}$ , (e)  $\text{Cu}_{\text{e},\text{ML}}$ , (f)  $\text{Cu}_{\text{e},\text{HL}}$ , (g)  $\text{CuO}_{\text{LL}}$ , (h)  $\text{CuO}_{\text{ML}}$ , (i)  $\text{CuO}_{\text{HL}}$ . Each graph shows the FE of the four gaseous products (left y-axis) with the average total current density for each of the applied potentials (right y-axis). Error bars represent one standard deviation for experiments repeated at least in triplicate.

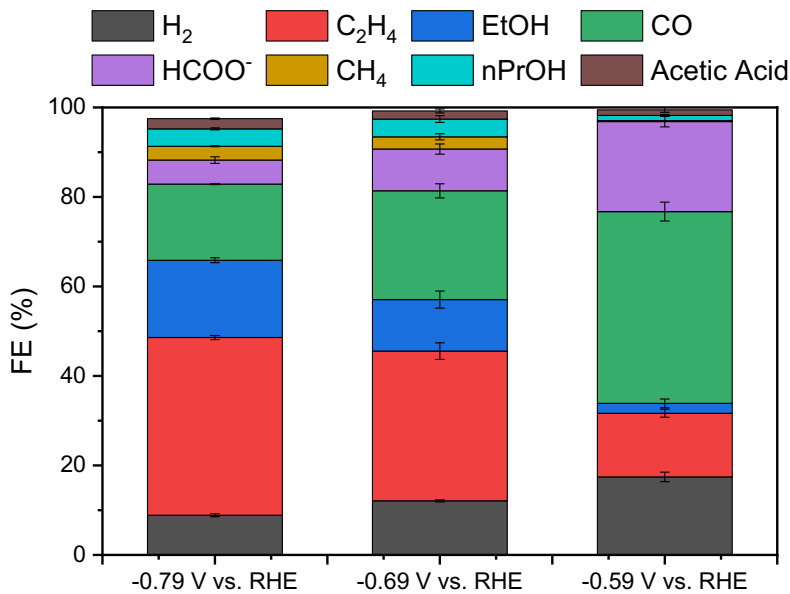


**Figure S9.** Total FE balance for Cu<sub>S,HL</sub> catalyst at E<sub>WE</sub> = -0.59, -0.69, and -0.79 V vs. RHE at 22 °C. Tables S6 and S7 provide the individual FE for each product. Error bars represent one standard deviation of triplicate experiments.

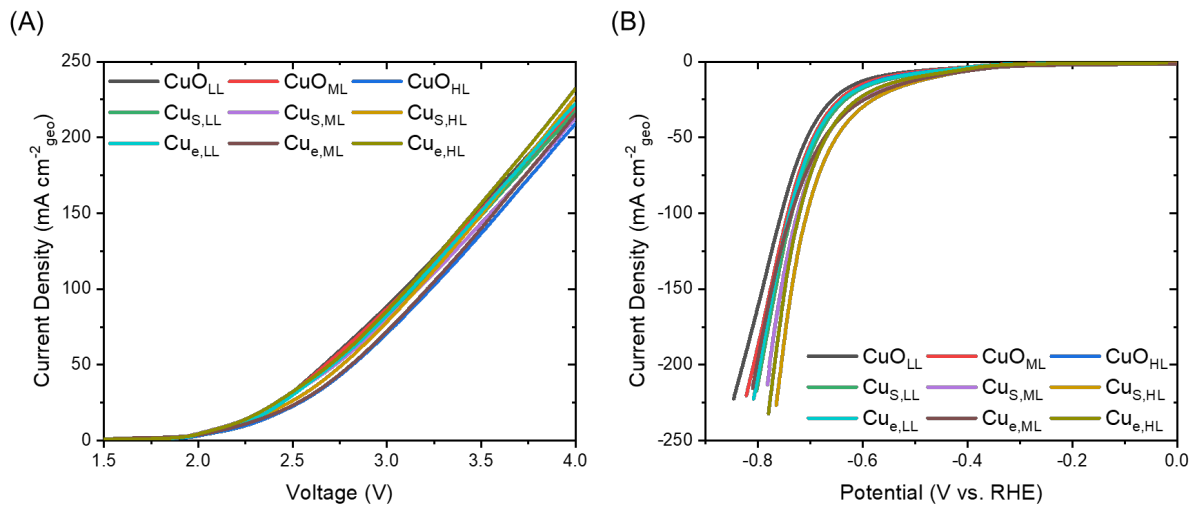


**Figure S10.** Full cell and working electrode electrochemical polarization curves for each electrocatalyst. (A) Full cell polarization curves [J<sub>geo</sub> vs. V<sub>op</sub>]. (B) Working electrode polarization curves [J<sub>geo</sub> vs. E<sub>WE</sub>].

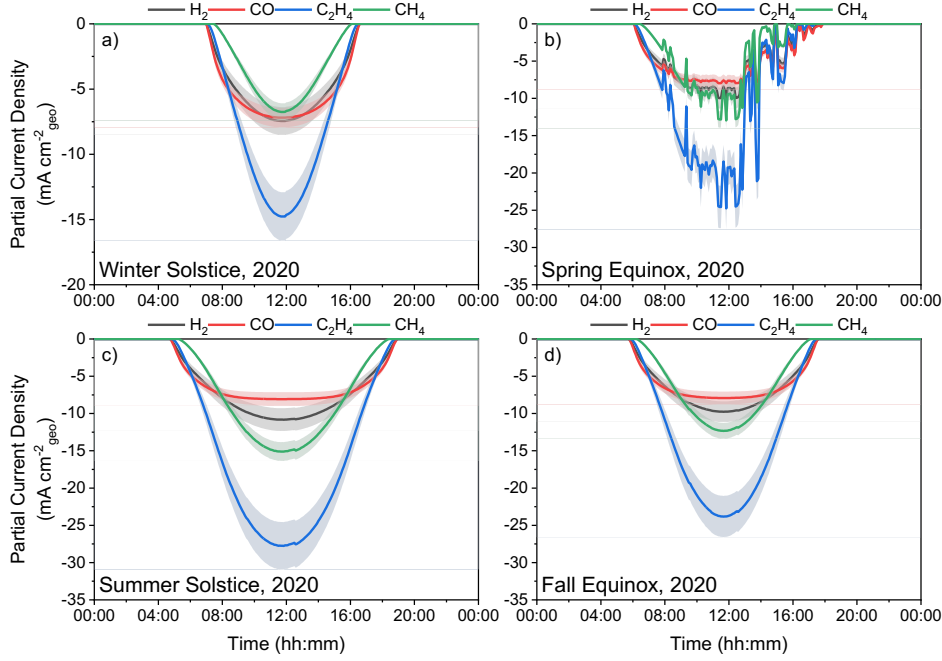


**Figure S11.** Modeling of the diurnal product output,  $J_x$ , of the Cu<sub>S,LL</sub> system for an Si PV with 350 mW maximum power output for four representative days throughout the year in Barstow, CA. (A) Winter solstice, (B) Spring equinox, (C) Summer solstice, (D) Fall equinox. Shaded regions represent error to one standard deviation.

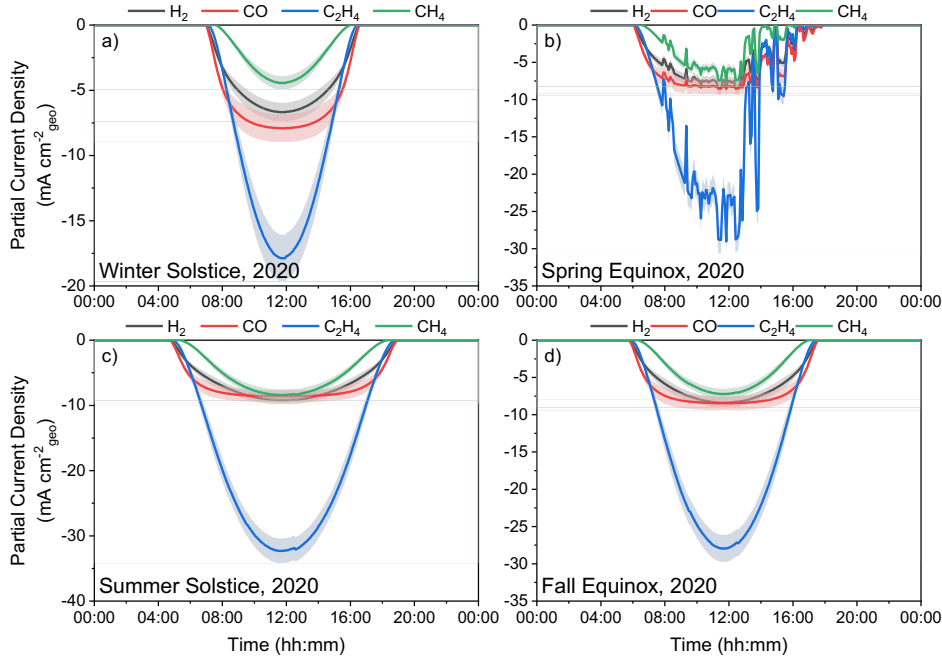


**Figure S12.** Modeling of the diurnal product output,  $J_x$ , of the Cu<sub>S,ML</sub> system for an Si PV with 350 mW maximum power output for four representative days throughout the year in Barstow, CA. (A) Winter solstice, (B) Spring equinox, (C) Summer solstice, (D) Fall equinox. Shaded regions represent error to one standard deviation.

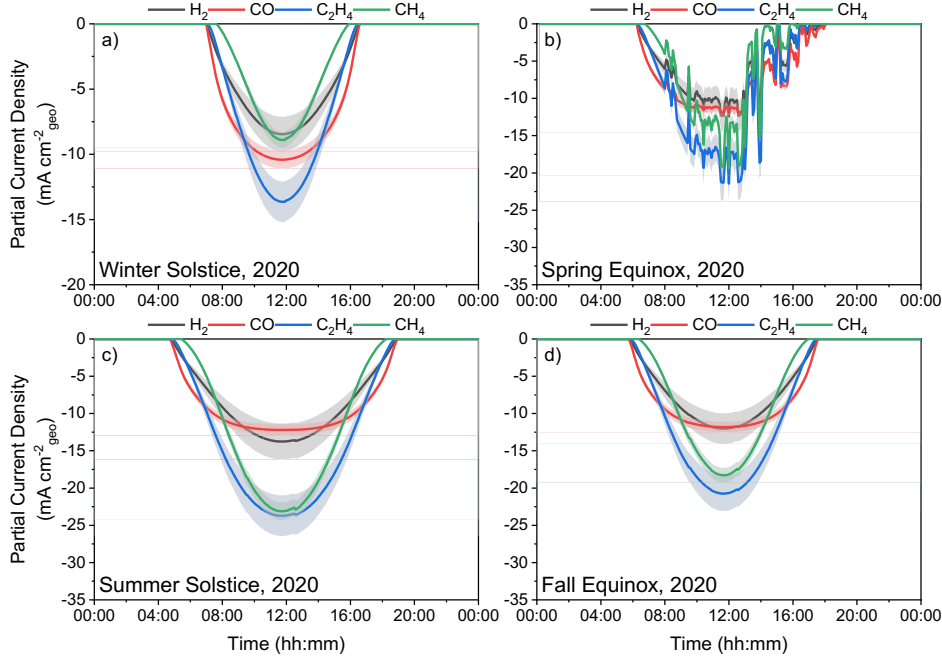


**Figure S13.** Modeling of the diurnal product output,  $J_x$ , of the  $\text{Cu}_{\text{e},\text{LL}}$  system for an Si PV with 350 mW maximum power output for four representative days throughout the year in Barstow, CA. (A) Winter solstice, (B) Spring equinox, (C) Summer solstice, (D) Fall equinox. Shaded regions represent error to one standard deviation.

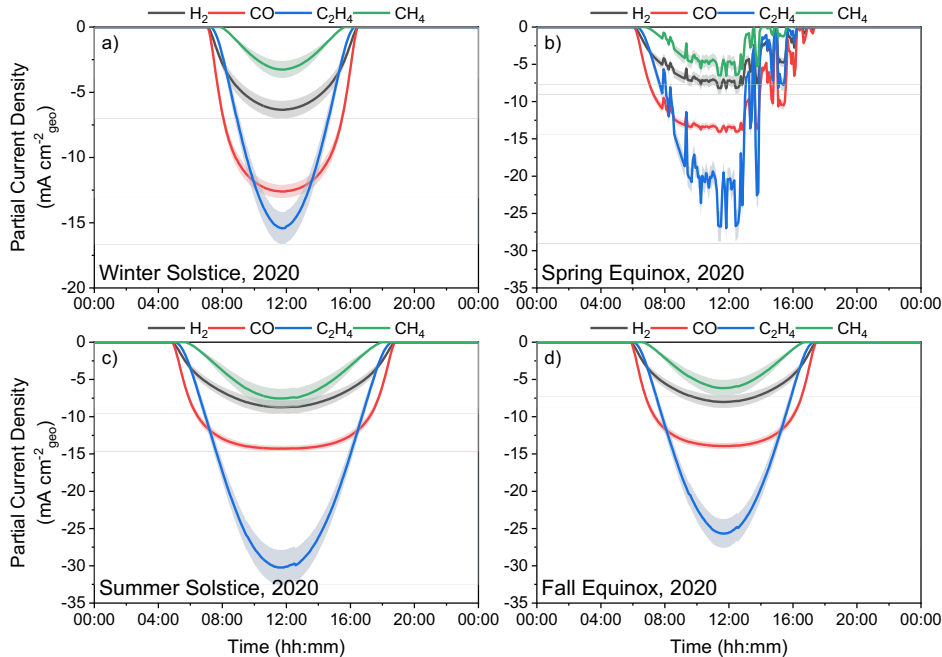


**Figure S14.** Modeling of the diurnal product output,  $J_x$ , of the  $\text{Cu}_{\text{e},\text{ML}}$  system for an Si PV with 350 mW maximum power output for four representative days throughout the year in Barstow, CA. (A) Winter solstice, (B) Spring equinox, (C) Summer solstice, (D) Fall equinox. Shaded regions represent error to one standard deviation.

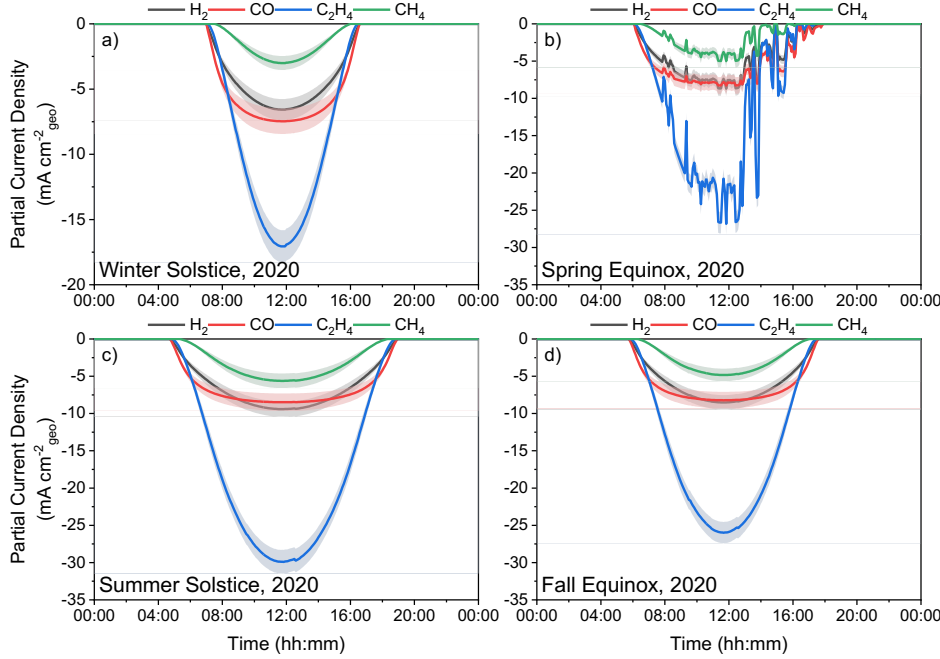


**Figure S15.** Modeling of the diurnal product output,  $J_x$ , of the  $\text{Cu}_{\text{e},\text{HL}}$  system for an Si PV with 350 mW maximum power output for four representative days throughout the year in Barstow, CA. (A) Winter solstice, (B) Spring equinox, (C) Summer solstice, (D) Fall equinox. Shaded regions represent error to one standard deviation.

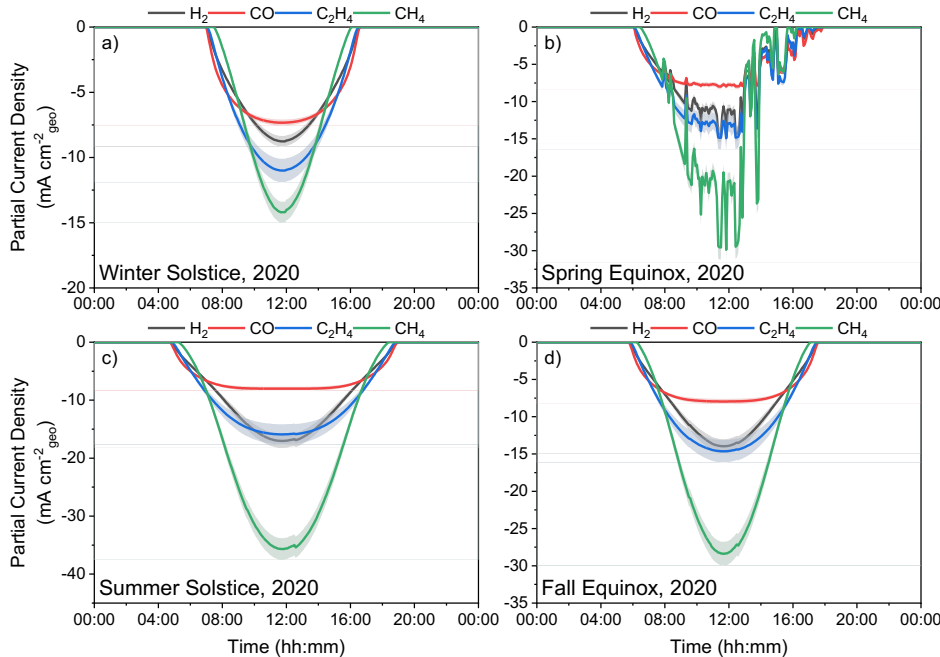


**Figure S16.** Modeling of the diurnal product output,  $J_x$ , of the  $\text{CuO}_{\text{LL}}$  system for an Si PV with 350 mW maximum power output for four representative days throughout the year in Barstow, CA. (A) Winter solstice, (B) Spring equinox, (C) Summer solstice, (D) Fall equinox. Shaded regions represent error to one standard deviation.

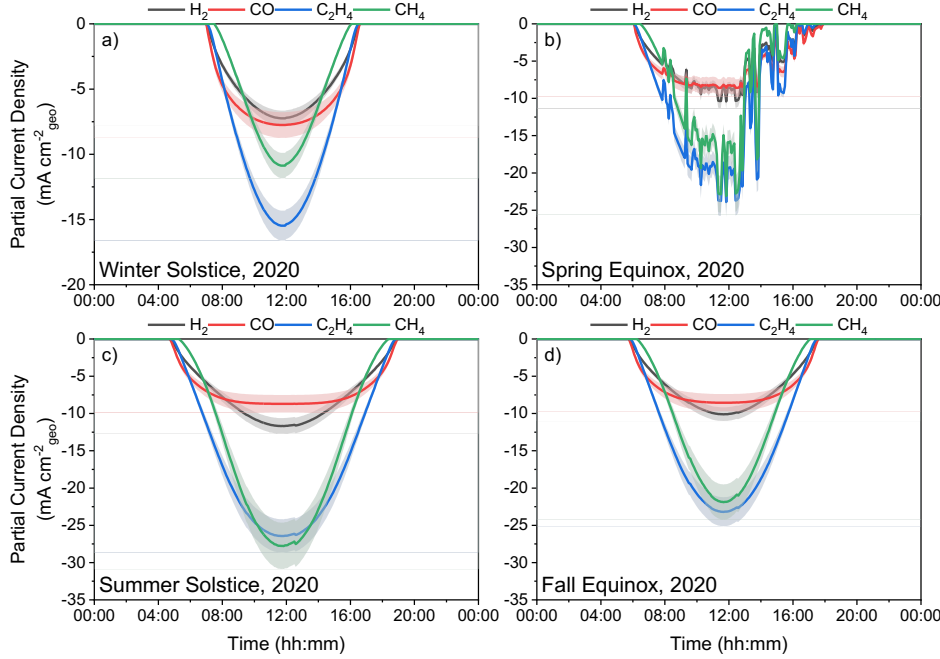


**Figure S17.** Modeling of the diurnal product output,  $J_x$ , of the CuO<sub>ML</sub> system for an Si PV with 350 mW maximum power output for four representative days throughout the year in Barstow, CA. (A) Winter solstice, (B) Spring equinox, (C) Summer solstice, (D) Fall equinox. Shaded regions represent error to one standard deviation.

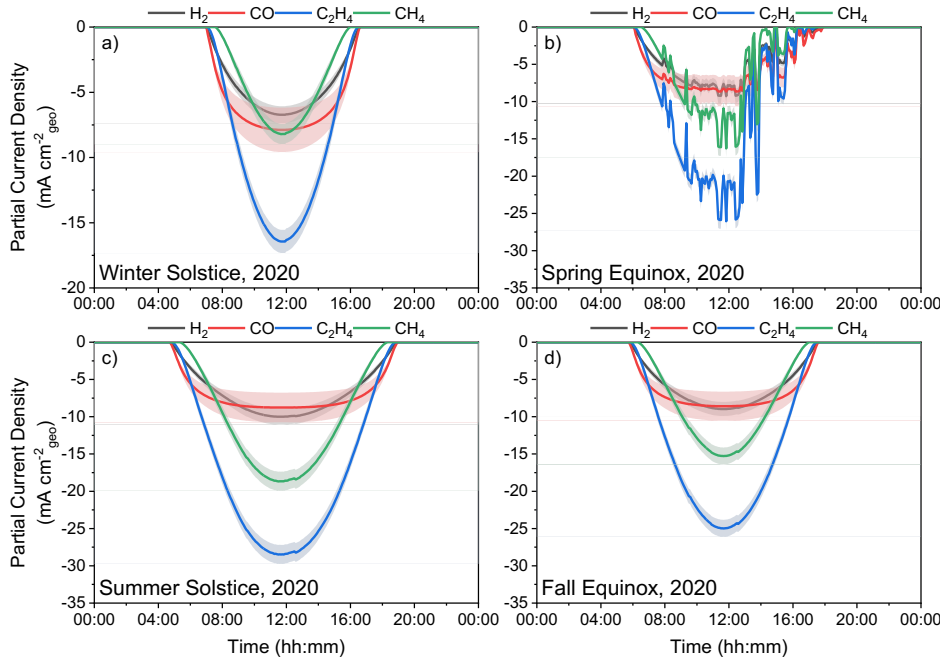


**Figure S18.** Modeling of the diurnal product output,  $J_x$ , of the CuO<sub>HL</sub> system for an Si PV with 350 mW maximum power output for four representative days throughout the year in Barstow, CA. (A) Winter solstice, (B) Spring equinox, (C) Summer solstice, (D) Fall equinox. Shaded regions represent error to one standard deviation.

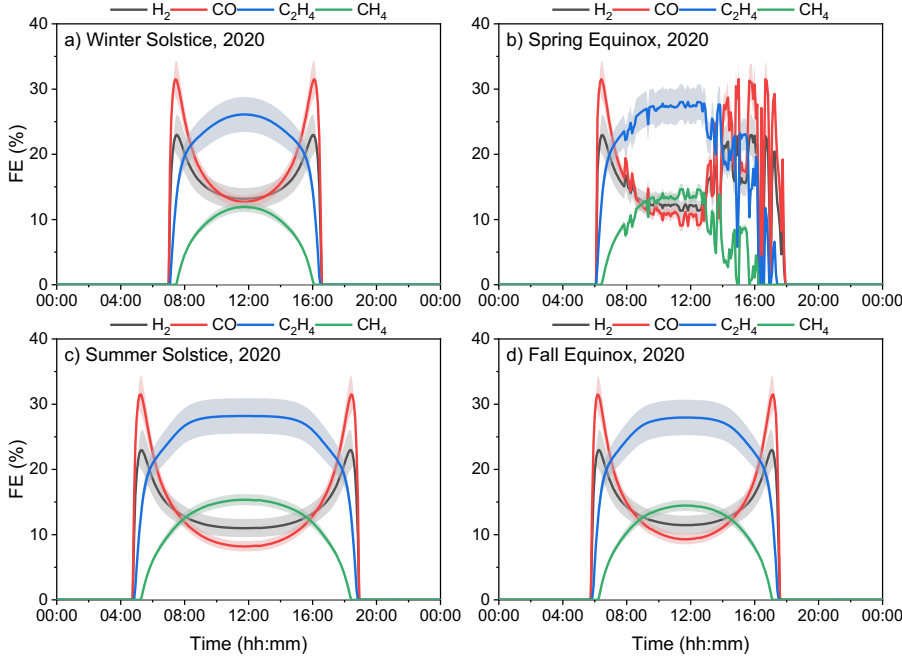


**Figure S19.** Modeling of the diurnal product selectivity, FE<sub>x</sub>, of the CuS,LL system for an Si PV with 350 mW maximum power output for four representative days throughout the year in Barstow, CA. (A) Winter solstice, (B) Spring equinox, (C) Summer solstice, (D) Fall equinox. Shaded regions represent error to one standard deviation.

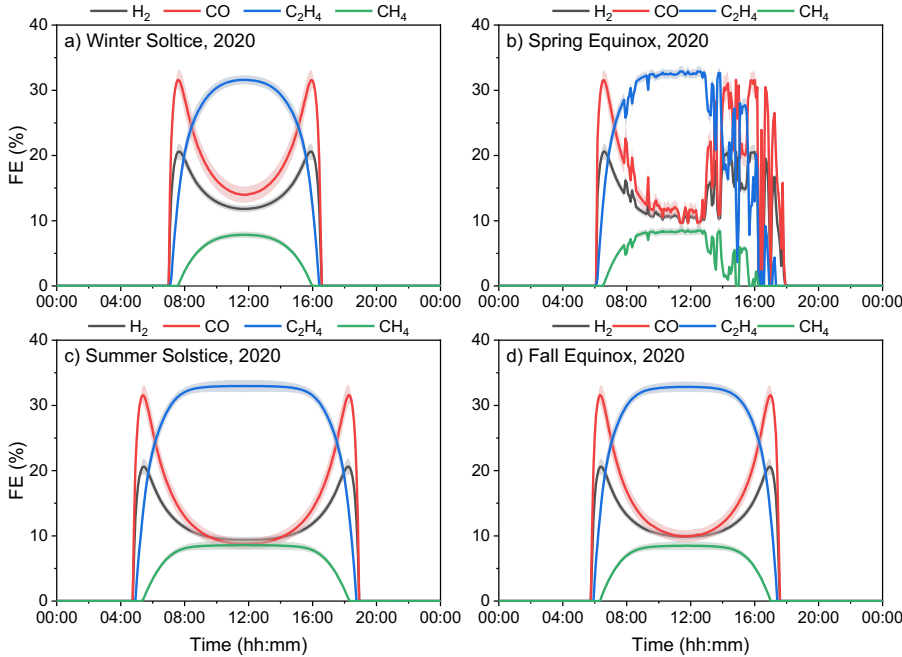


**Figure S20.** Modeling of the diurnal product selectivity, FE<sub>x</sub>, of the CuS,ML system for an Si PV with 350 mW maximum power output for four representative days throughout the year in Barstow, CA. (A) Winter solstice, (B) Spring equinox, (C) Summer solstice, (D) Fall equinox. Shaded regions represent error to one standard deviation.

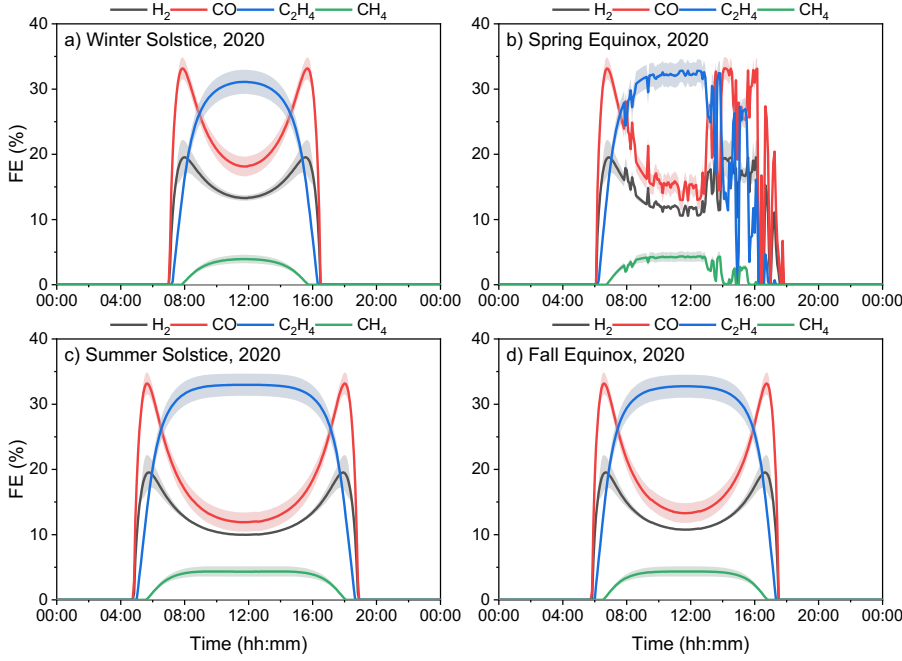


**Figure S21.** Modeling of the diurnal product selectivity, FE<sub>x</sub>, of the Cu<sub>S,HL</sub> system for an Si PV with 350 mW maximum power output for four representative days throughout the year in Barstow, CA. (A) Winter solstice, (B) Spring equinox, (C) Summer solstice, (D) Fall equinox. Shaded regions represent error to one standard deviation.

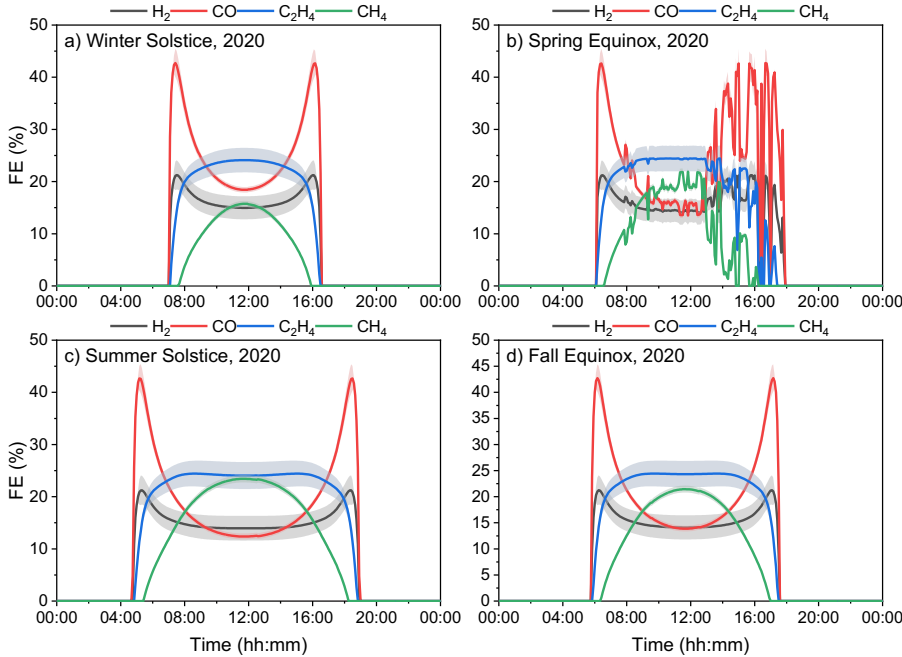


**Figure S22.** Modeling of the diurnal product selectivity, FE<sub>x</sub>, of the Cu<sub>e,LL</sub> system for an Si PV with 350 mW maximum power output for four representative days throughout the year in Barstow, CA. (A) Winter solstice, (B) Spring equinox, (C) Summer solstice, (D) Fall equinox. Shaded regions represent error to one standard deviation.

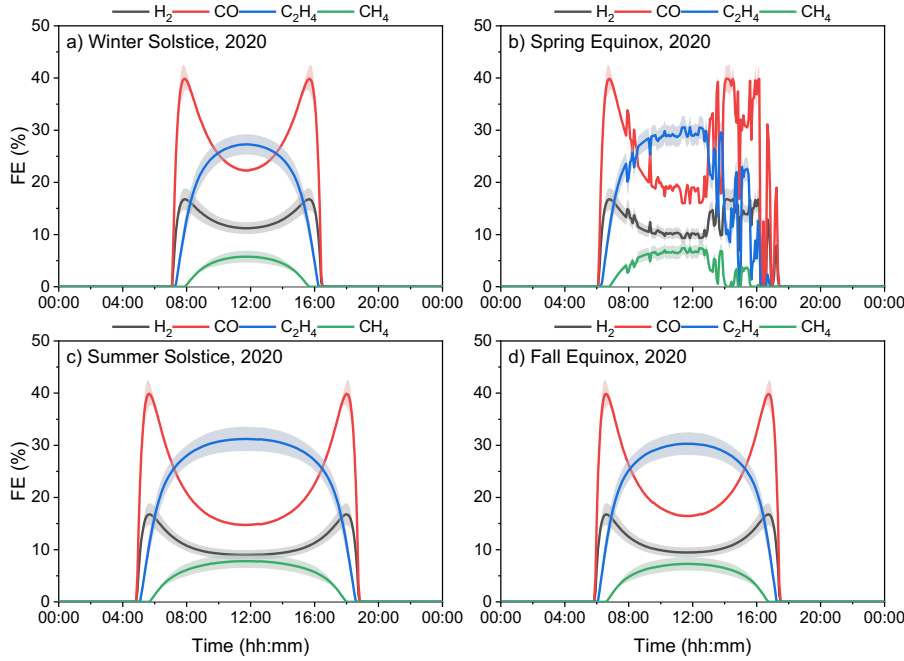


**Figure S23.** Modeling of the diurnal product selectivity, FE<sub>x</sub>, of the Cu<sub>e</sub>,ML system for an Si PV with 350 mW maximum power output for four representative days throughout the year in Barstow, CA. (A) Winter solstice, (B) Spring equinox, (C) Summer solstice, (D) Fall equinox. Shaded regions represent error to one standard deviation.

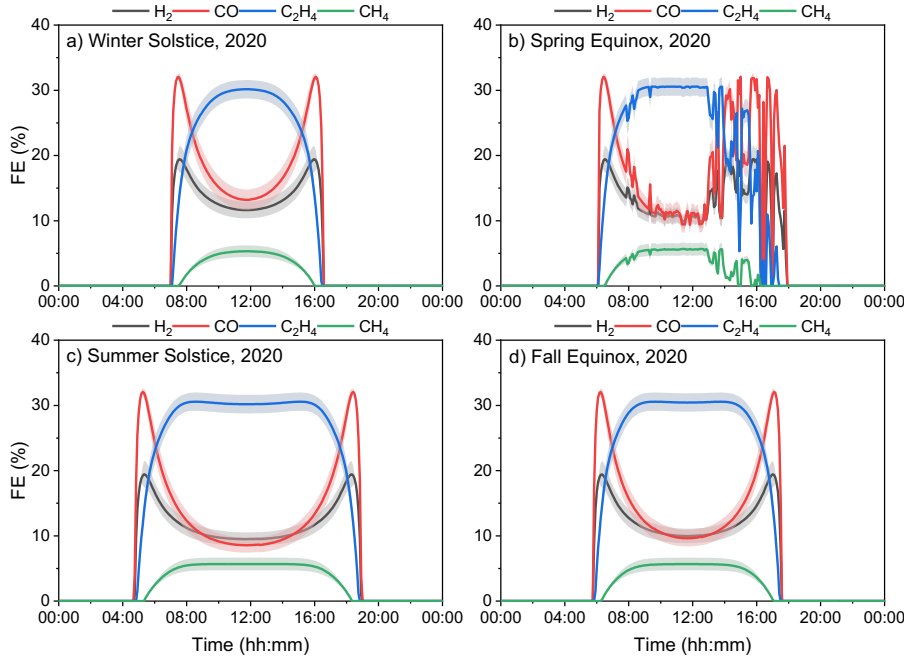


**Figure S24.** Modeling of the diurnal product selectivity, FE<sub>x</sub>, of the Cu<sub>e</sub>,HL system for an Si PV with 350 mW maximum power output for four representative days throughout the year in Barstow, CA. (A) Winter solstice, (B) Spring equinox, (C) Summer solstice, (D) Fall equinox. Shaded regions represent error to one standard deviation.

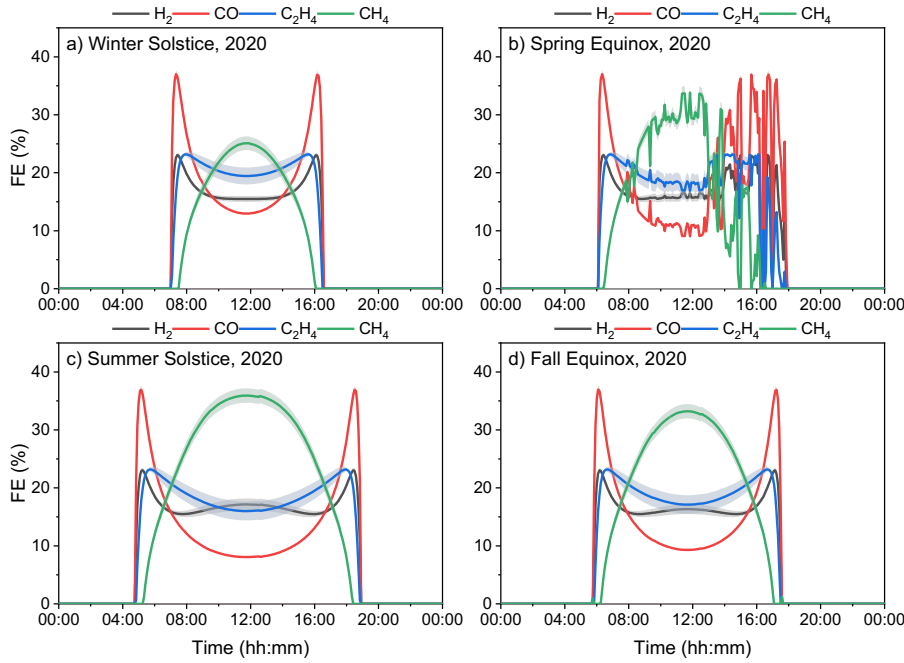


**Figure S25.** Modeling of the diurnal product selectivity,  $FE_x$ , of the CuO<sub>LL</sub> system for an Si PV with 350 mW maximum power output for four representative days throughout the year in Barstow, CA. (A) Winter solstice, (B) Spring equinox, (C) Summer solstice, (D) Fall equinox. Shaded regions represent error to one standard deviation.

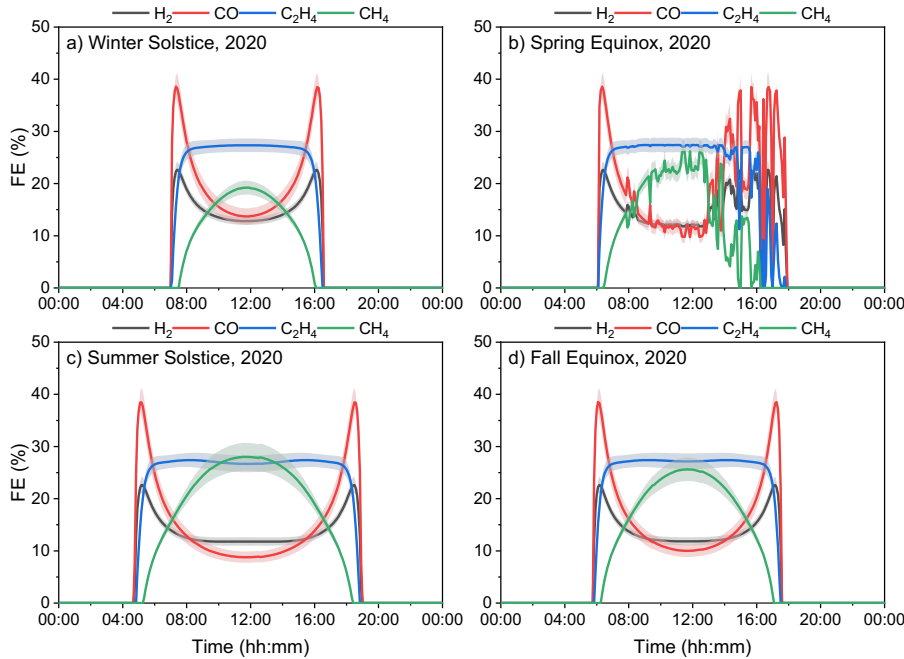


**Figure S26.** Modeling of the diurnal product selectivity,  $FE_x$ , of the CuO<sub>ML</sub> system for an Si PV with 350 mW maximum power output for four representative days throughout the year in Barstow, CA. (A) Winter solstice, (B) Spring equinox, (C) Summer solstice, (D) Fall equinox. Shaded regions represent error to one standard deviation.

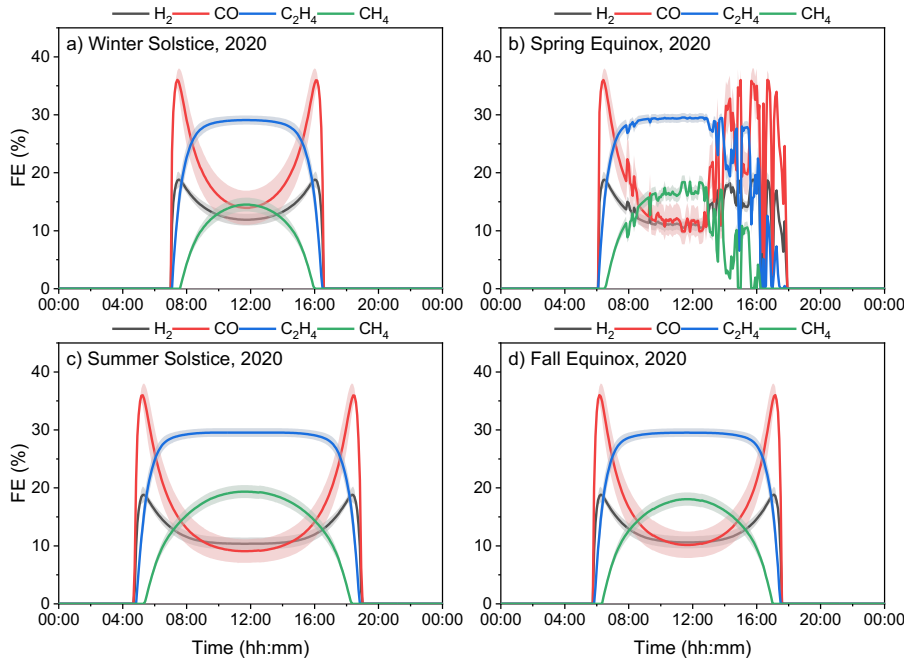


**Figure S27.** Modeling of the diurnal product selectivity,  $FE_x$ , of the CuO<sub>HL</sub> system for an Si PV with 350 mW maximum power output for four representative days throughout the year in Barstow, CA. (A) Winter solstice, (B) Spring equinox, (C) Summer solstice, (D) Fall equinox. Shaded regions represent error to one standard deviation.

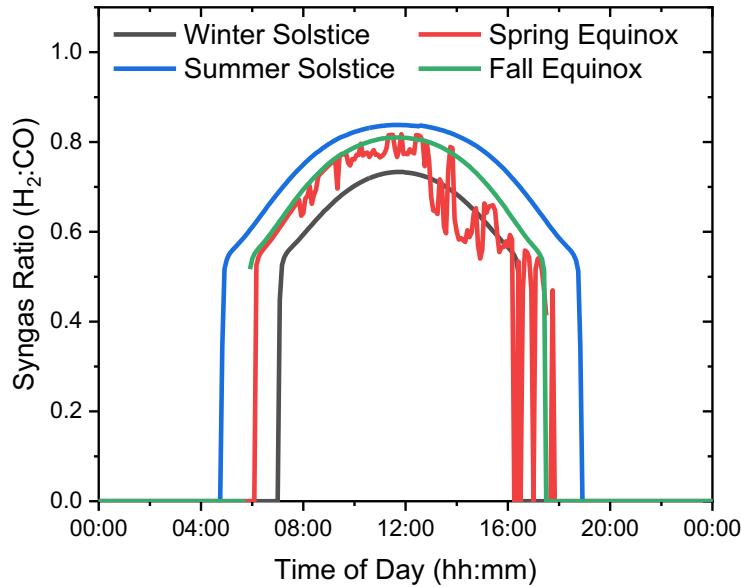


**Figure S28.** Ratio of H<sub>2</sub>:CO (syngas) produced throughout the day for the four representative days throughout the year in Barstow, CA, when irradiation effects only are considered. A nominal range of 0.6 – 0.8 is maintained for this ratio and is similar to the ratio of syngas generated by coal gasification.<sup>4,5</sup>

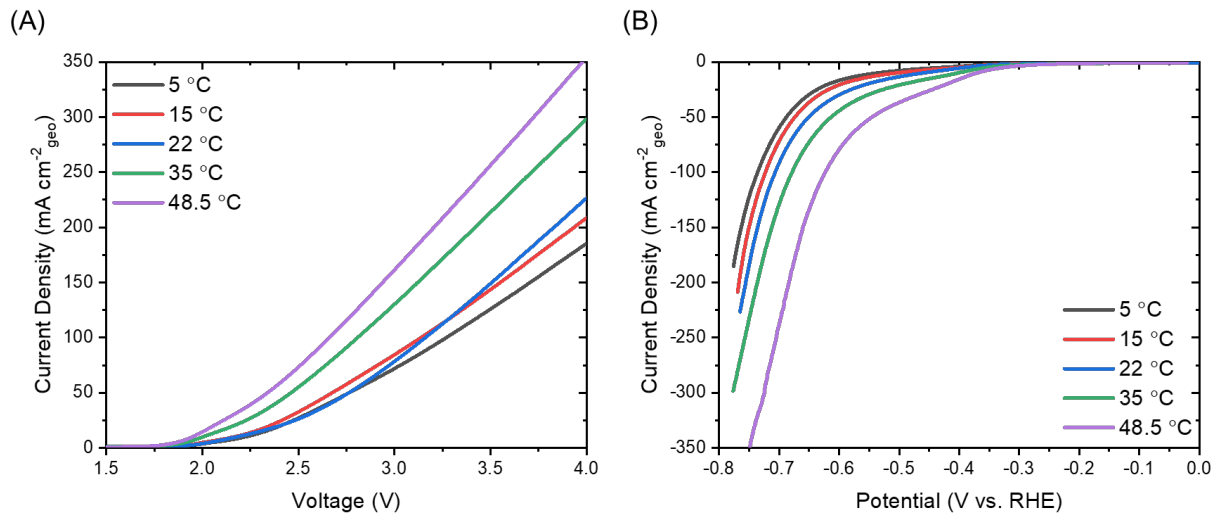


**Figure S29.** Experimental full cell and working electrode electrochemical polarization curves for the CuS,HL system at bulk electrolyte temperatures of: 5 °C, 15 °C, 22 °C, 35 °C, and 48.5 °C. (A) Full cell polarization curves. (B) Working electrode polarization curves.

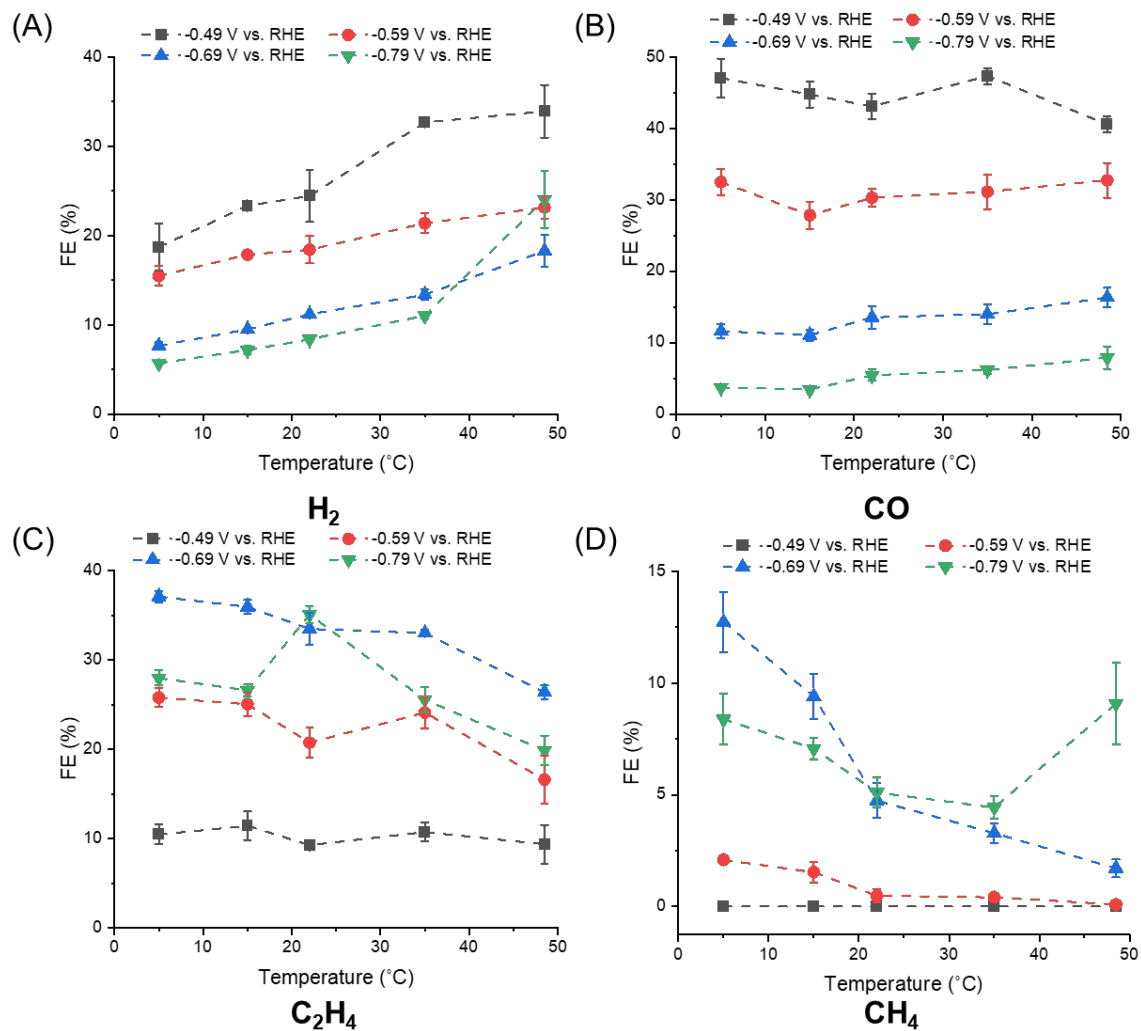


**Figure S30.** Comparison of FE to operating temperature for each of the four gas products at four applied potentials: -0.49, -0.59, -0.69, -0.79 V vs. RHE. (A) H<sub>2</sub>, (B) CO, (C) C<sub>2</sub>H<sub>4</sub>, (D) CH<sub>4</sub>. Error bars represent one standard deviation for experiments repeated at least in triplicate.

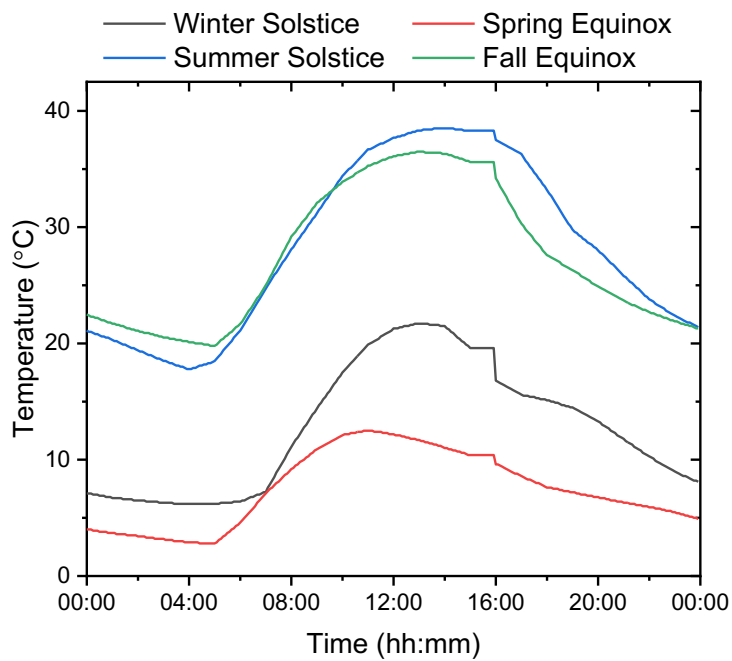


**Figure S31.** Ambient temperatures recorded at Barstow, CA over a 24-hour period during the Winter Solstice, Spring Equinox, Summer Solstice, and Fall Equinox in 2020.

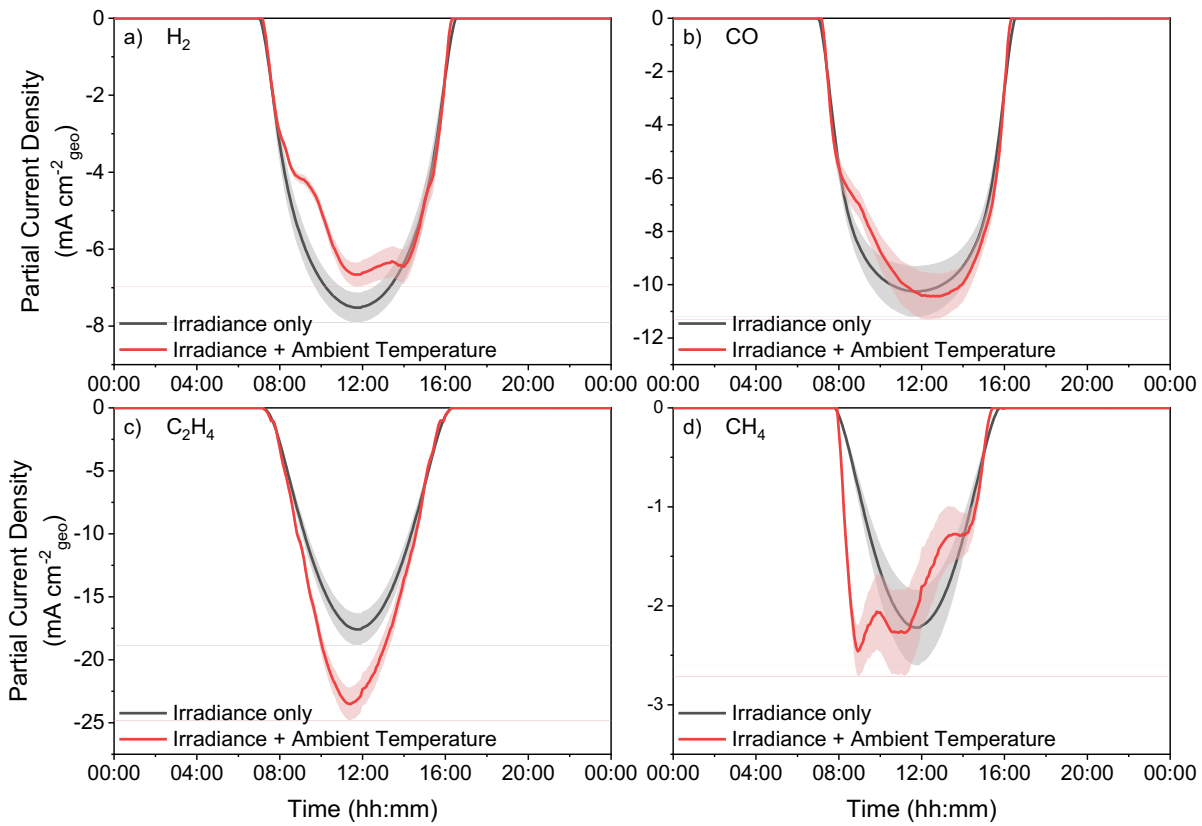


**Figure S32.** Comparison of the diurnal output of the Cu<sub>S,HL</sub> system during the Winter solstice, when only irradiance is considered vs. when irradiance and ambient temperature catalyst effects are considered. Note that temperature effects for PV performance are considered in both cases. Data shown corresponds to the gaseous products, (A) H<sub>2</sub>, (B) CO, (C) C<sub>2</sub>H<sub>4</sub>, and (D) CH<sub>4</sub>. Shaded regions represent error to one standard deviation.

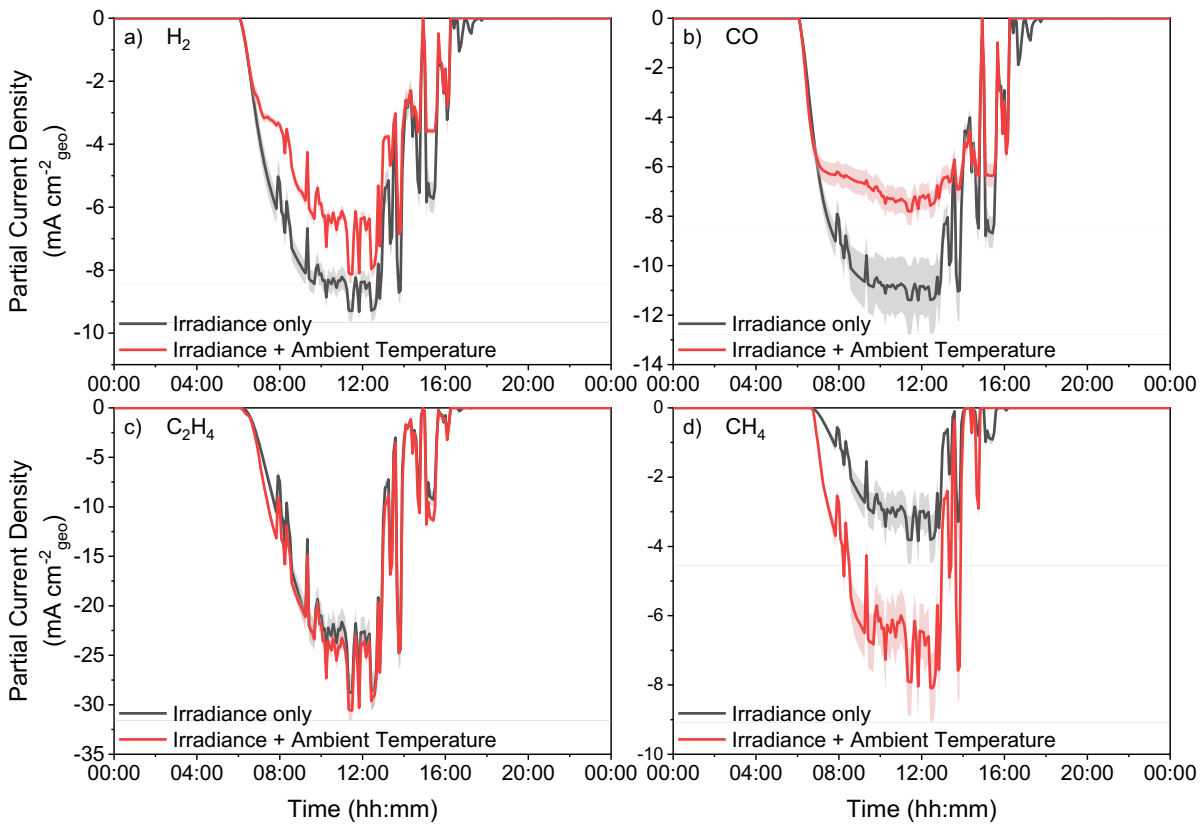


**Figure S33.** Comparison of the diurnal output of the Cu<sub>S,HL</sub> system during the Spring equinox, when only irradiance is considered vs. when irradiance and ambient temperature catalyst effects are considered. Note that temperature effects for PV performance are considered in both cases. Data shown corresponds to the gaseous products, (A) H<sub>2</sub>, (B) CO, (C) C<sub>2</sub>H<sub>4</sub>, and (D) CH<sub>4</sub>. Shaded regions represent error to one standard deviation.

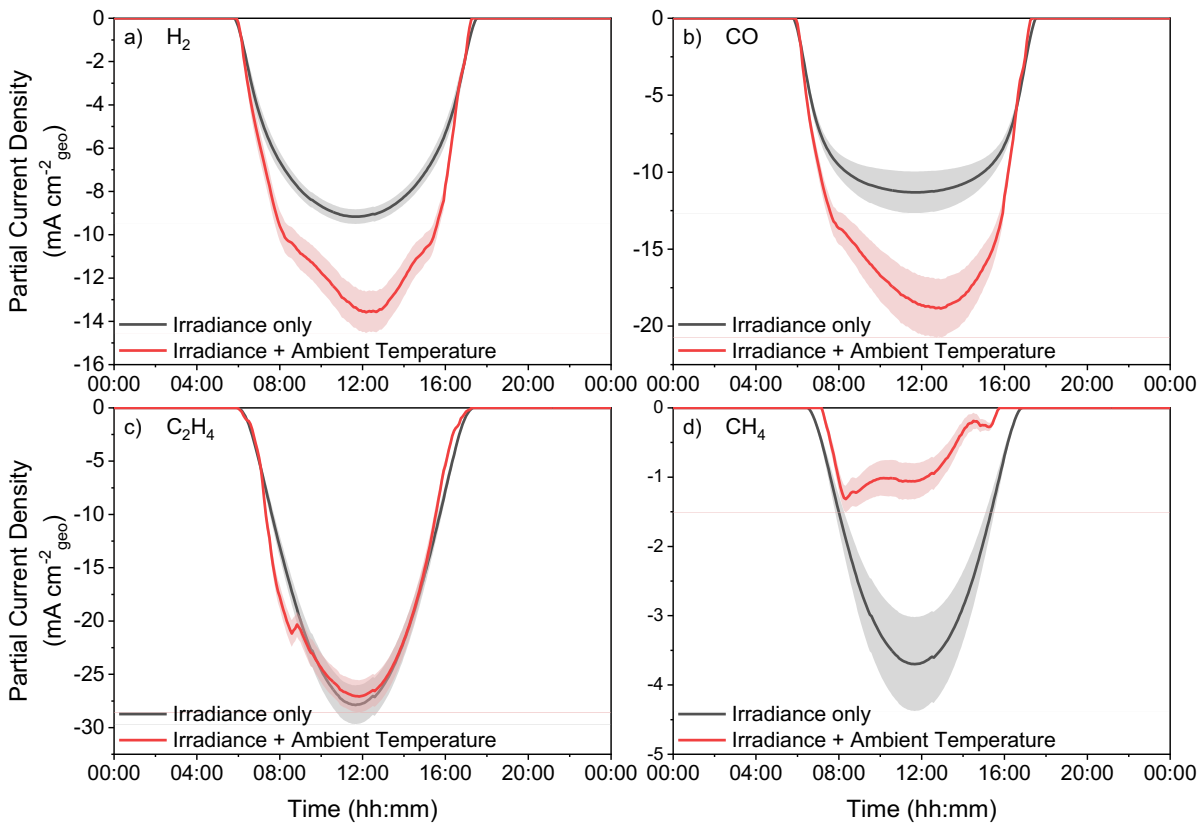


**Figure S34.** Comparison of the diurnal output of the Cu<sub>S,HL</sub> system during the Fall equinox, when only irradiance is considered vs. when irradiance and ambient temperature catalyst effects are considered. Note that temperature effects for PV performance are considered in both cases. Data shown corresponds to the gaseous products, (A) H<sub>2</sub>, (B) CO, (C) C<sub>2</sub>H<sub>4</sub>, and (D) CH<sub>4</sub>. Shaded regions represent error to one standard deviation.

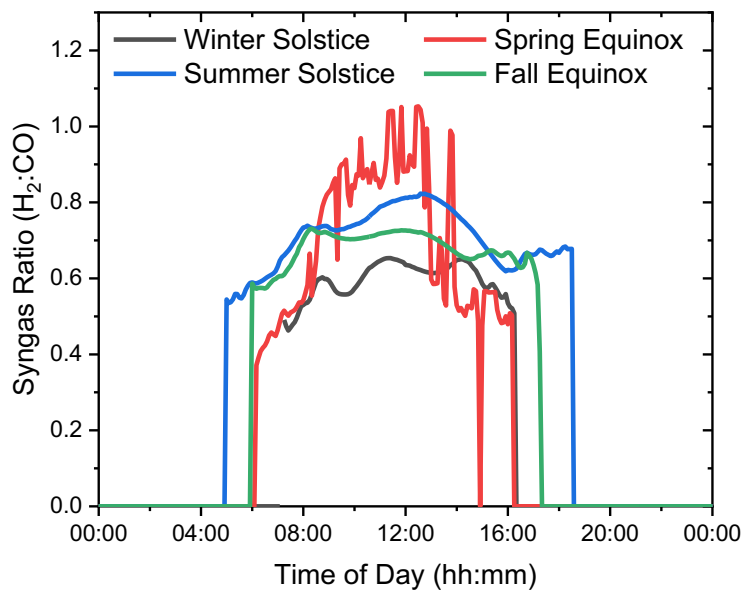
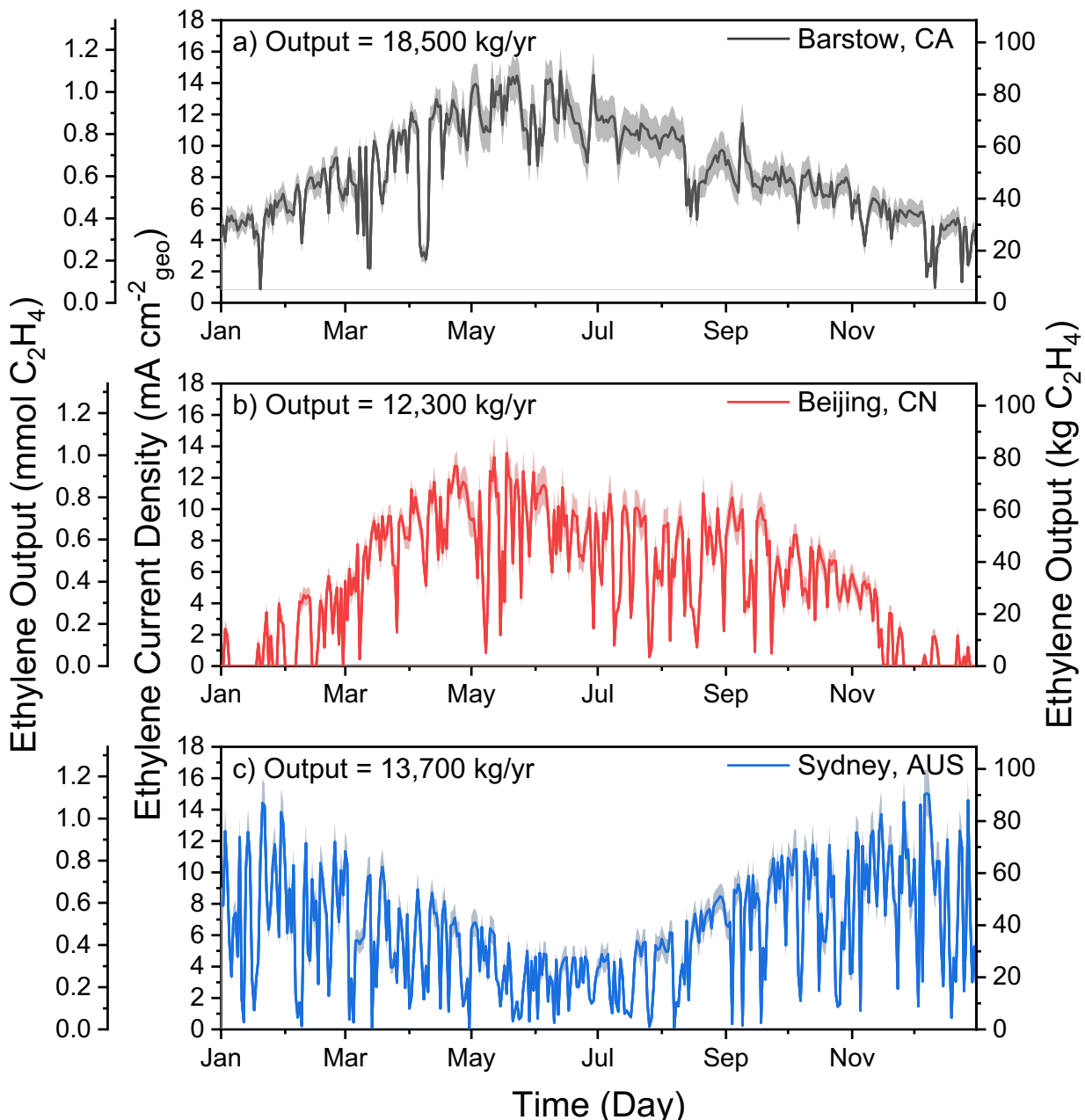


**Figure S35.** Ratio of H<sub>2</sub>:CO (syngas) produced throughout the day for the four representative days throughout the year in Barstow, CA, where both temperature and irradiation effects are considered. A nominal range of 0.6 – 1.0 is maintained for this ratio and is similar to the ratio of syngas generated by coal gasification.<sup>4,5</sup>



\*Note: Data points correspond to the average output from a 24-hr period

**Figure S36.** Annual modeled output of the Cu<sub>S,HL</sub> PV-EC CO<sub>2</sub>R device for the locations of: (A) Barstow, CA; (B) Beijing, CN; (C) Sydney, AUS. The two left y-axes correspond to ethylene output (mA cm<sup>-2</sup> and mmol C<sub>2</sub>H<sub>4</sub>) for a single 1 cm<sup>2</sup> electrochemical device and the right y-axis corresponds to the ethylene generation (kg C<sub>2</sub>H<sub>4</sub>) of a PV-EC CO<sub>2</sub>R device scaled to a 1 MW solar farm. Shaded regions represent error to one standard deviation.

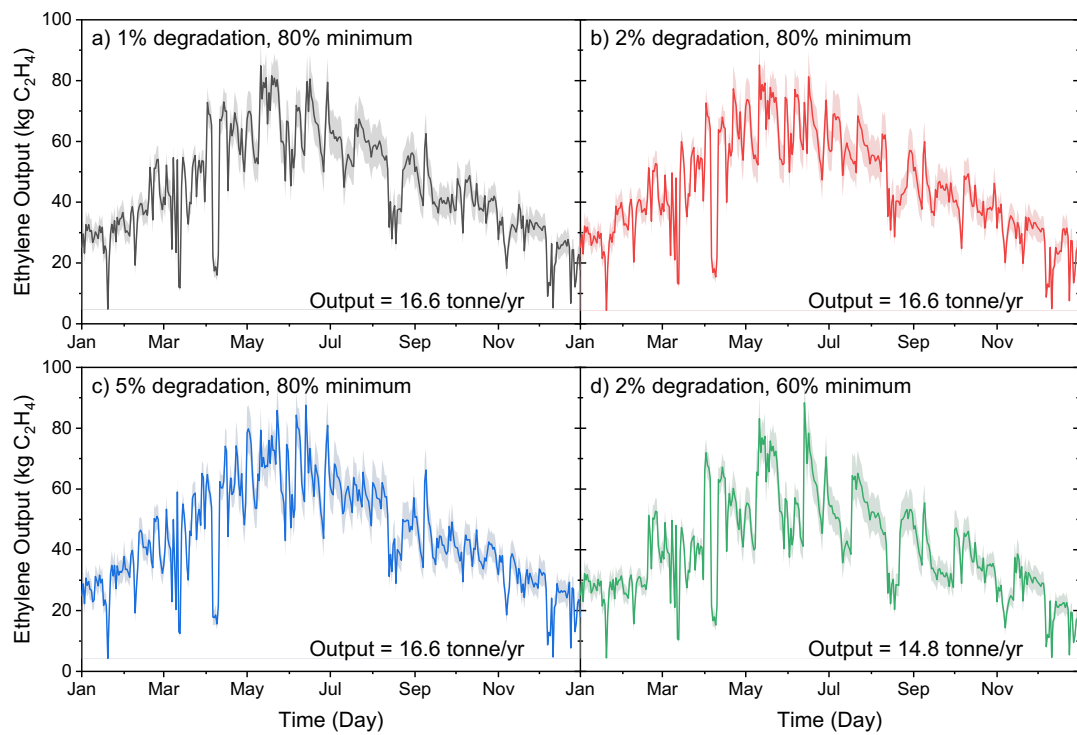


**Figure S37.** Comparison of ethylene output for the CuS.HL catalyst used in a PV-EC CO<sub>2</sub>R device located in Barstow, CA, with varying hypothetical rates of ethylene degradation and minimum relative thresholds at which the catalyst is replaced. (A) 1% degradation per 24 h + 80% minimum threshold, (B) 2% degradation per 24 h + 80% minimum threshold, (C) 5% degradation per 24 h + 80% minimum threshold, (D) 2% degradation per 24 h + 60% minimum threshold. Shaded regions represent error to one standard deviation.

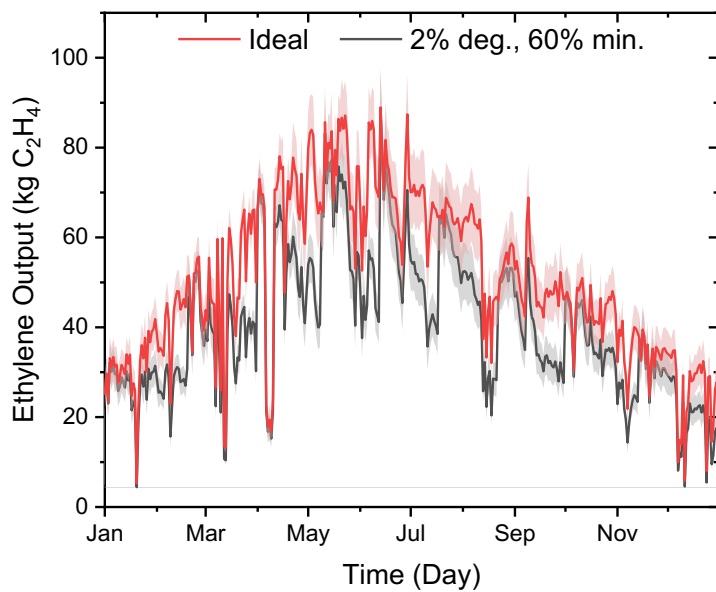


**Figure S38.** Performance of the modeled PV-EC CO<sub>2</sub>R device using the Cu<sub>S,HL</sub> catalyst and located in Barstow, CA, under ideal conditions and at a 2% ethylene degradation rate with a 60% minimum relative threshold at which the catalyst is replaced. Shaded regions represent error to one standard deviation.

### Supplementary Tables

**Table S1.** Description of the deposition techniques used for the nine Cu-based catalysts. The samples are referenced by their target chemical composition (e.g., Cu), the deposition technique (e.g., S = sputtering), and their relative loading (e.g., LL = lowest loading).

Sample Name	Deposition Conditions
Cu <sub>S,LL</sub>	Cu sputtering: - Power: 50 W - Time: 600 s
Cu <sub>S,ML</sub>	Cu sputtering: - Power: 100 W - Time: 600 s
Cu <sub>S,HL</sub>	Cu sputtering: - Power: 200 W - Time: 600 s
Cu <sub>e,LL</sub>	Cu e-beam deposition: - Thickness: 50 nm - Deposition rate: 1 Å/s
Cu <sub>e,ML</sub>	Cu e-beam deposition: - Thickness: 100 nm - Deposition rate: 1 Å/s
Cu <sub>e,HL</sub>	Cu e-beam deposition: - Thickness: 200 nm - Deposition rate: 1 Å/s
CuO <sub>LL</sub>	Reactive oxide sputtering: - Cu sputtered at 40 W for 900 s - O <sub>2</sub> flow rate = 4 sccm - Ar flow rate = 20 sccm
CuO <sub>ML</sub>	Reactive oxide sputtering: - Cu sputtered at 100 W for 450 s - O <sub>2</sub> flow rate = 4 sccm - Ar flow rate = 20 sccm
CuO <sub>HL</sub>	Reactive oxide sputtering: - Cu sputtered at 200 W for 230 s - O <sub>2</sub> flow rate = 4 sccm - Ar flow rate = 20 sccm

**Table S2.** Annual modeled gaseous product output of nine electrocatalysts for a 1 cm<sup>2</sup> electrochemical device and Si PV with 350 mW maximum power output when only irradiation variations are considered for Barstow, CA in 2020. Error represents one standard deviation.

Sample	H <sub>2</sub> (mol)	H <sub>2</sub> error (mol)	CO (mol)	CO error (mol)	C <sub>2</sub> H <sub>4</sub> (mol)	C <sub>2</sub> H <sub>4</sub> error (mol)	CH <sub>4</sub> (mol)	CH <sub>4</sub> error (mol)
Cu <sub>S,LL</sub>	0.523	0.180	0.491	0.105	0.177	0.036	0.126	0.014
Cu <sub>S,ML</sub>	0.465	0.076	0.538	0.139	0.209	0.030	0.077	0.011
Cu <sub>S,HL</sub>	0.508	0.132	0.689	0.104	0.205	0.026	0.038	0.007
Cu <sub>e,LL</sub>	0.604	0.177	0.712	0.087	0.160	0.030	0.012	0.177
Cu <sub>e,ML</sub>	0.436	0.177	0.712	0.087	0.184	0.026	0.038	0.008
Cu <sub>e,HL</sub>	0.460	0.117	0.514	0.129	0.197	0.031	0.052	0.012
CuO <sub>LL</sub>	0.666	0.034	0.502	0.023	0.125	0.012	0.281	0.022
CuO <sub>ML</sub>	0.524	0.069	0.534	0.141	0.182	0.022	0.217	0.019
CuO <sub>HL</sub>	0.474	0.074	0.543	0.248	0.192	0.027	0.155	0.024

**Table S3.** Diurnal product output for the Cu<sub>S,HL</sub> catalyst under conditions of variable incident irradiation (Barstow, CA, 2020). Values correspond to a photovoltaic with a maximum power output of 350 mW and a cathode geometric area of 1 cm<sup>2</sup>. Error corresponds to one standard deviation. The daily production here is defined as the integral of the productivity over 24 h converted to a mole basis.

Season	H <sub>2</sub> (μmol)	H <sub>2</sub> error	CO (μmol)	CO error	C <sub>2</sub> H <sub>4</sub> (μmol)	C <sub>2</sub> H <sub>4</sub> error	CH <sub>4</sub> (μmol)	CH <sub>4</sub> error
Winter solstice (12/21)	0.94	0.07	1.38	0.11	0.29	0.02	0.05	0.01
Summer solstice (6/20)	1.87	0.09	2.44	0.26	0.83	0.06	0.16	0.03
Spring equinox (3/19)	1.13	0.07	1.58	0.15	0.42	0.03	0.08	0.01
Fall equinox (9/22)	1.45	0.08	1.95	0.20	0.59	0.04	0.11	0.02

**Table S4.** Diurnal product output for the Cu<sub>S</sub>,HL catalyst under conditions of variable incident irradiation and ambient temperature (Barstow, CA, 2020). Values correspond to a photovoltaic with a maximum power output of 350 mW and a cathode geometric area of 1 cm<sup>2</sup>. Error corresponds to one standard deviation.

Season	H <sub>2</sub> (μmol)	H <sub>2</sub> error	CO (μmol)	CO error	C <sub>2</sub> H <sub>4</sub> (μmol)	C <sub>2</sub> H <sub>4</sub> error	CH <sub>4</sub> (μmol)	CH <sub>4</sub> error
Winter solstice (12/21)	0.82	0.05	1.36	0.10	0.37	0.02	0.06	0.01
Summer solstice (6/20)	2.77	0.19	3.82	0.35	0.85	0.05	0.05	0.01
Spring equinox (3/19)	0.84	0.03	1.15	0.08	0.45	0.02	0.18	0.02
Fall equinox (9/22)	2.05	0.15	2.97	0.27	0.59	0.04	0.03	0.01

**Table S5.** Annual production of gaseous products for a 1 MW solar farm at the locations of Barstow, CA; Beijing, CN; Sydney, AUS.

	H <sub>2</sub> (tonne/yr)	CO (tonne/yr)	C <sub>2</sub> H <sub>4</sub> (tonne/yr)	CH <sub>4</sub> (tonne/yr)
Barstow, CA	3.6	70.8	18.5	1.4
Beijing, CN	2.2	45.8	12.3	1.1
Sydney, AUS	2.3	48.5	13.7	1.2

**Table S6.** Individual faradaic efficiencies for gaseous products corresponding to Figure S9. Error indicates one standard deviation.

V vs. RHE	Gas products							
	H <sub>2</sub> FE (%)	H <sub>2</sub> error	C <sub>2</sub> H <sub>4</sub> FE (%)	C <sub>2</sub> H <sub>4</sub> error	CO FE (%)	CO error	CH <sub>4</sub> FE (%)	CH <sub>4</sub> error
-0.59	17.4	1.1	14.2	0.9	42.9	2.1	0.2	0.0
-0.69	12.1	0.2	33.5	1.9	24.3	1.6	2.7	0.7
-0.79	8.9	0.4	39.7	0.5	17.0	0.1	3.1	0.1

**Table S7.** Individual faradaic efficiencies for liquid products corresponding to Figure S9. Error indicates one standard deviation.

V vs. RHE	Liquid products							
	EtOH FE (%)	EtOH error	HCOO <sup>-</sup> FE (%)	HCOO <sup>-</sup> error	nPrOH FE (%)	nPrOH error	Acetic acid FE (%)	Acetic acid error
-0.59	2.2	1.0	20.1	1.2	1.2	0.2	1.3	0.6
-0.69	11.5	1.9	9.3	1.1	4.0	0.8	1.8	0.4
-0.79	17.3	0.5	5.4	0.7	3.9	0.2	2.3	0.2

### Supplementary References

- (1) Faiman, D. Assessing the Outdoor Operating Temperature of Photovoltaic Modules. *Progress in Photovoltaics: Research and Applications* **2008**, *16* (4), 307–315. <https://doi.org/10.1002/pip.813>.
- (2) Biesinger, M. C.; Payne, B. P.; Grosvenor, A. P.; Lau, L. W. M.; Gerson, A. R.; Smart, R. St. C. Resolving Surface Chemical States in XPS Analysis of First Row Transition Metals, Oxides and Hydroxides: Cr, Mn, Fe, Co and Ni. *Applied Surface Science* **2011**, *257* (7), 2717–2730. <https://doi.org/10.1016/j.apsusc.2010.10.051>.
- (3) Biesinger, M. C. Advanced Analysis of Copper X-Ray Photoelectron Spectra. *Surface and Interface Analysis* **2017**, *49* (13), 1325–1334. <https://doi.org/10.1002/sia.6239>.
- (4) Źogała, A. Equilibrium Simulations of Coal Gasification – Factors Affecting Syngas Composition. *Journal of Sustainable Mining* **2014**, *13* (2), 30–38. <https://doi.org/10.7424/jsm140205>.
- (5) Adnan, M. A.; Hidayat, A.; Hossain, M. M.; Muraza, O. Transformation of Low-Rank Coal to Clean Syngas and Power via Thermochemical Route. *Energy* **2021**, *236*, 121505. <https://doi.org/10.1016/j.energy.2021.121505>.